ACS Catalysis

pubs.acs.org/acscatalysis
Research Article

Optimization Method Based on Simplex for Surface Area Improved Photocatalytic Performance of g-C_3N_4

Matevž Roškarič, Janez Zavašnik, Dániel Zámbó, Tomaž Kotnik, Sebastijan Kovačič, Gregor Žerjav,* and Albin Pintar

Cite This: *ACS Catal.* 2023, 13, 13282–13300

ABSTRACT: The main objective of the present study was to increase the specific surface area (S_{BET}) of graphitic carbon nitride (g-C_3N_4) prepared from dicyandiamide by effectively modifying the synthesis procedure using the Simplex optimization method. A remarkable increase in S_{BET} was achieved in only a few steps, with the highest value of 86 m^2/g. Compared to the reference material, the improved photocatalyst exhibited enhanced and unique structural, textural, optical, and electronic properties, reflected in the improved ability of the photocatalyst to degrade a variety of organic pollutants dissolved in water. By performing scavenger and spin-trapping experiments, it was confirmed that the major reactive oxygen species formed under visible-light illumination of the enhanced photocatalyst were singlet oxygen ($^1O_2$) and superoxide anion radicals ($O_2^{-\bullet}$) with a purposed formation mechanism. The enhanced formation of $^1O_2$ enabled high activity and stability of the optimized materials as well as selective response to degradation of the pharmaceutical compounds studied. By using the simple and fast Simplex optimization algorithm to determine new synthesis parameters, we obtained an improved g-C_3N_4 that completely degrades bisphenol A under the conditions studied.

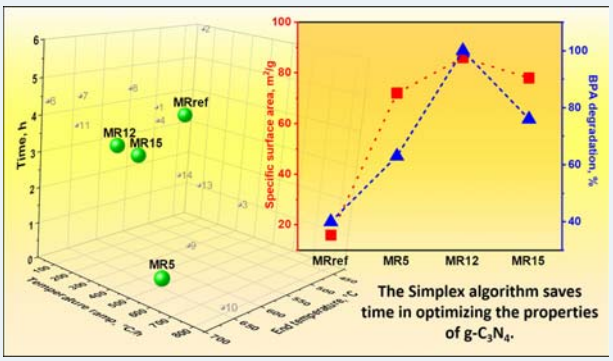

KEYWORDS: *simplex, g-C_3N_4, heterogeneous photocatalysis, reactive oxygen species, visible- and solar-light illumination*

1. INTRODUCTION

In recent years, interest in heterogeneous photocatalysis has shifted to more environmentally friendly organic semiconductors like graphitic carbon nitride (g-C_3N_4).[1] g-C_3N_4 has proven to be low-cost, relatively thermally stable, and capable of degrading water-dissolved organic pollutants (dyes, bisphenols, phenols, etc.) under visible-light illumination. It exhibits a high photocatalytic energy conversion due to the "exotic" layered structure.[2] This makes g-C_3N_4 a hot-topic material in the photocatalysis research field.[3,4] The main drawback of g-C_3N_4 is its low specific surface area;[1] in addition, its charge carrier recombination rate is also high.[5] For this reason, new strategies and concepts are increasingly being applied, such as volume photocatalysis, which combines the principles of heterogeneous and homogeneous catalysis. In these methods, the reactants can penetrate the bulk of the photocatalyst, e.g., g-C_3N_4, at room temperature and react with the existing photogenerated holes. This allows a larger amount of photogenerated electrons to migrate to the surface of g-C_3N_4 and form reactive oxygen species or participate in the reduction reactions to form hydrogen from biomass-derived formic acid.[6−8] This double-reaction "attack" strategy significantly improved the photocatalytic activity. However, the suitable properties of the catalyst, e.g., an imperfect two-dimensional (2D) structure bound by intermolecular hydrogen bonds or the van der Waals force, must be taken into account to allow the interception of holes/electrons from the reactant (acceptor/donor) and the migration of the remaining electrons/holes to the surface of the catalyst.[6] Therefore, developing new synthesis procedures to prepare g-C_3N_4 with a high specific surface area (S_{BET}) is essential. As for the possible scale-up of the synthesis procedure, a facile, one-pot method is favorable, such as a simple thermal polycondensation without any pre-, mid-, or postsynthetic modification or additional steps.

Typically, a step-by-step approach alias univariate optimization is used, where one parameter is changed, and all of the others are kept constant. Consequently, this does not allow us to study the interactions between parameters. Hence, the optimal parameters are rarely found, and usually, only local extremes can be found, in addition to a long and expensive

Received: July 24, 2023
Revised: September 20, 2023
Published: September 29, 2023

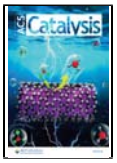

https://doi.org/10.1021/acscatal.3c03394
ACS Catal. 2023, 13, 13282−13300

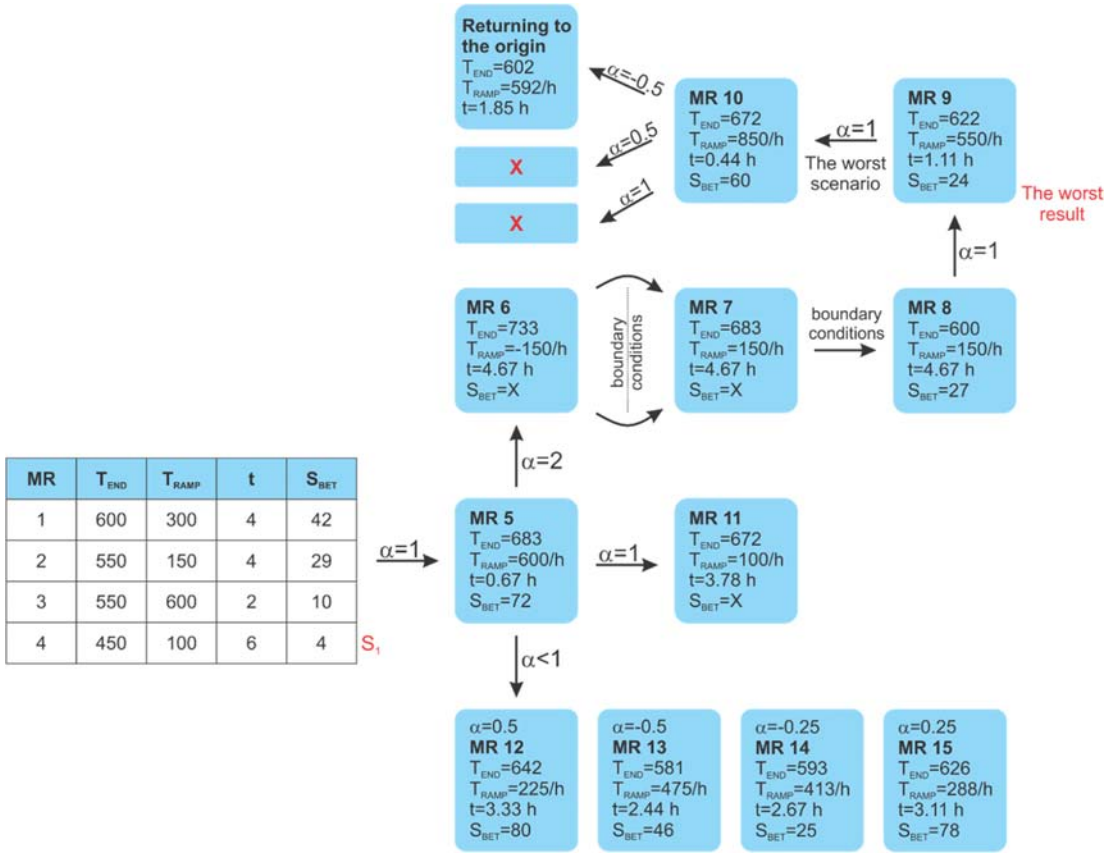

MR	T_{END}	T_{RAMP}	t	S_{BET}
1	600	300	4	42
2	550	150	4	29
3	550	600	2	10
4	450	100	6	4

Figure 1. Schematic overview of the Simplex optimization process with the synthesis conditions for each point. The table on the left represents the four starting experiments (metric space) that were needed for the optimization process (MR1−4 samples). Different Simplex optimization scenarios (refer to the Supporting Information (SI) for a detailed description) and different selected factors and movements were used to obtain the new experimental parameters (blue brackets).

optimization process.[9,10] Therefore, the usage of a chemometric approach to determine the optimal conditions is recommended, with its usage increasing in all research fields over the past years.[9−13] Simplex optimization is one of the fastest and most straightforward approaches that do not require specific software.[9,10] Additionally, Nelder and Mead improved the basic Simplex procedure to obtain a more flexible optimization procedure.[9,14] Yasmin et al.[12] used a basic RMS approach (Simplex) to optimize the photocatalytic degradation setup. Using Simplex optimization, they determined the optimal pH value, time, and concentration of the photocatalyst for enhancing the removal of chemical oxygen demand (COD) and NH_4^+-N. Chemometric approaches, such as Simplex, could also be used to improve the synthesis procedures of materials. Khummongkol et al.[15] utilized the Simplex method to optimize the activated carbon synthesis for iodine adsorption. Using the Simplex method, they determined the optimal parameters in only a few steps. Gracia Soto et al.[11] used the Simplex method to design the optimal synthesis conditions to obtain the LTA zeolite with relative crystallinity as the response criteria. The investigated conditions were the molar ratios of components, crystal growth time, reaction time, and reaction temperature. They obtained the optimal synthesis parameters in only 24 steps, which resulted in the formation of zeolite with a relative crystallinity of 95.4% compared with the commercially available material. Recently, Wrzecionek et al.[16] and Cortés-Borda et al.[17] used the Simplex optimization method to optimize poly(glycerol succinate) and Carpanone synthesis procedures. However, to our knowledge, no fast and simple Simplex optimization method has yet been used to improve the synthesis of g-C_3N_4 or other semiconductors using only a simple one-step synthesis approach without the use of computer programs.

Therefore, the main objective of the research work presented here was to optimize the parameters of the one-step g-C_3N_4 synthesis procedure[5] using dicyandiamide to obtain g-C_3N_4 with a higher specific surface area for enhanced photocatalytic reaction under visible-light and simulated sunlight illumination. To achieve this goal, we used the modified Simplex method to find the global maximum in only a few steps. Compared to classical parameter optimization, this allowed us to significantly reduce the time and resources needed for optimization. The synthesized photocatalysts were thoroughly characterized using a variety of surface, texture, electronic, and optical sensitive techniques, e.g., solid-state nuclear magnetic resonance (NMR), electron paramagnetic resonance (EPR), Fourier transform infrared (FTIR), transmission electron microscopy (TEM), photoluminescence spectroscopy, time-correlated single photon counting, and photocurrent measurements. To investigate the possibility of wastewater remediation, the photocatalysts were tested for the degradation of selected bisphenols and pharmaceutical compounds under visible-light and simulated sunlight illumination. Furthermore, the active species responsible for the photochemical degradation of organic pollutants dissolved in water were monitored by using electron paramagnetic

https://doi.org/10.1021/acscatal.3c03394
ACS Catal. 2023, 13, 13282−13300

spectroscopy in addition to an optical and fluorometric approach.

2. EXPERIMENTAL SECTION

2.1. Simplex Synthesis Application. All chemicals used for the synthesis were of analytical grade and used without further purification. In all cases, ultrapure water (18.2 MΩ cm) was used. A facile calcination was used to synthesize the g-C_3N_4 photocatalyst from dicyandiamide (DCDA, Sigma-Aldrich) in a muffle furnace (Nabertherm LT 9/11/SKM, Germany). The DCDA was put in an alumina crucible covered with a lid and heated with the appropriate temperature program (Figure 1). The temperature program was obtained using the Simplex optimization method (end temperature, the temperature ramp, and the time of calcination). Therefore, four experiments were needed, from which the worst point was used as the reflection point (MR1−4). The goal of the optimization was to increase the specific surface area (fitness function). The synthesized photocatalysts were denoted as MRx (x = 1−15), with the corresponding synthesis parameters shown in Figure 1 and Table S1. For a more detailed explanation of the Simplex synthesis procedure, please refer to the Supporting Information (Chapter 1. Simplex optimization method). A reference g-C_3N_4 sample denoted as MRref was synthesized by using DCDA and synthesis parameters (550, 300 °C/h, 4 h) from the literature.[5,18] Additionally, a commercially available g-C_3N_4 sample (TCI, TCI Chemicals) was used for comparison in selected characterization.

2.2. Determination of the Surface and Textural Properties of Solids. The specific surface area and pore size distribution of the investigated materials were measured by nitrogen physisorption at −196 °C (Micromeritics, model TriStar II 3020). Fourier-transformed IR (FTIR) spectra of the materials were recorded with a PerkinElmer Frontier FTIR spectrometer. The solid-state NMR spectroscopy was performed on a Bruker Avance 400 MHz spectrometer. The phase composition and crystallinity of the prepared materials were determined by using powder X-ray diffraction analysis (PANalytical, model PRO MPD). Transmission electron microscopy (TEM) was employed to obtain TEM micrographs (JEOL Inc., model JEM-2100). A Micromeritics' AutoChem II 2920 apparatus and CO_2 and O_2 temperature-programmed desorption (TPD) analyses were employed to determine the amount/strength of basic surface sites and oxygen consumption. The surface acidic properties were determined using pyridine TPD analysis and a PerkinElmer Pyris 1 TGA analyzer. The thermogravimetric analysis of the prepared materials carried out in an air atmosphere was performed by using a PerkinElmer Pyris 1 TGA analyzer. Zeta potential measurements were performed using an Ultra Red zetasizer (Malvern Panalytical). Detailed information about the surface and textural characterization techniques is provided in the Supporting Information.

2.3. Determination of the Optical and Electronic Properties of Solids. UV−vis diffuse reflectance (UV−vis-DR) spectra of the investigated g-C_3N_4 photocatalysts were obtained by employing a Lambda 35 UV−vis spectrophotometer (PerkinElmer). The solid-state photoluminescence (PL), charge carrier decay, and pure absorption measurements were performed by using an Edinburgh FS5 spectrofluorometer from Edinburgh Instruments. The phosphorescence was measured on the FL-QM (Horiba) and the quantum yield (QY) on the Fluoromax+ (Horiba) instruments. The photoresponse characteristic, electrochemical impedance spectroscopy (EIS), and cyclic voltammetry (CV) measurements were obtained by using a Metrohm Autolab PGSTAT302N potentiostat/galvanostat and a three-electrode electrochemical cell. X-band electron paramagnetic resonance (EPR) spectra were obtained by using an Adani CMS8400 EPR spectrometer. Detailed information about instrumental techniques for the determination of optical and electronic properties of solids is provided in the Supporting Information.

2.4. Photocatalytic Oxidation Runs. The photocatalytic oxidation of aqueous solutions of bisphenols (bisphenol A (BPA), bisphenol F (BPF), bisphenol AF (BPAF), bisphenol S (BPS)) and pharmaceutical compounds (paracetamol (PARA), acetylsalicylic acid (ASA), salicylic acid (SA), benzoic acid (BA), and caffeine (CAFF)) was performed in a batch slurry reactor (Lenz Laborglas) under either visible-light (halogen 150 W lamp, Philips) or simulated solar-light (Scientech, model SciSun SN0002642) irradiation. Quenching and reusability experiments were performed by using the same experimental setup. The degradation of the model pollutants was followed by using either HPLC LC-40 (Shimadzu) or HPLC Spectra (Thermo Scientific) instruments equipped with a UV−vis detection system and appropriate analysis conditions for each model pollutant. The total organic carbon (TOC) content in aqueous-phase samples was determined using a Shimadzu TOC-L analyzer equipped with an ASI-L autosampler; synthetic air (Messer, purity 5.0) was used as an oxidizing agent. The carbon, hydrogen, and nitrogen content in fresh and used photocatalyst samples was determined using a PerkinElmer CHNS 2400 Series II analyzer. Detailed information is provided in the Supporting Information.

2.5. Mechanistic Study of the Generation of Reactive Oxygen Species under Visible-Light Illumination. Using a photoluminescence method (PerkinElmer, model LS 55) and the probe molecule coumarin (Alfa Aesar), we evaluated the hydroxyl radical ($OH^•$) formation tendency of the investigated materials. Utilizing a PerkinElmer Lambda 465 UV−vis spectrophotometer, 2,2′-azino-bis(3-ethylbenzothiazoline-6-sulfonic acid) (ABTS, Sigma), and $K_2S_2O_8$ (Aldrich), we determined the tendency of the examined materials toward the generation of electrons (e^-) and/or superoxide anion radicals ($O_2^{-•}$). The spin-trapping experiments using either 2,2,6,6-tetramethylpiperidine (TEMP, Sigma-Aldrich) or 5−5-dimethyl-1-pyrroline-*N*-oxide (DMPO, Sigma-Aldrich), dissolved in ultrapure water, or dimethyl sulfoxide (DMSO, Sigma-Aldrich) were carried out in a flat cell using an Adani CMS8400 EPR spectrometer. Detailed information can be found in the Supporting Information.

3. RESULTS AND DISCUSSION

The aim of the present study was to use DCDA as a precursor and a simple one-step thermal g-C_3N_4 synthesis with a Simplex optimization method (simple Excel calculations) to obtain g-C_3N_4 with the highest specific surface area and consequently enhanced photocatalytic activity (see the SI for Simplex theory or synthesis application). Using the Simplex optimization technique, we obtained "exotic" synthesis parameters (Figure 1) that no one would normally think of using (e.g., the final temperature of 642 °C, temperature ramp of 413 °C/h, duration of 2.44 h, etc.). These "exotic" and equally "harsh" parameters made it possible to obtain an improved g-C_3N_4 photocatalyst without any postsynthesis modifications, as the

https://doi.org/10.1021/acscatal.3c03394
ACS Catal. 2023, 13, 13282−13300

synthesis parameters calculated by the Simplex method (Table S1) could affect the polymerization process (polycondensation) and thus the surface area, texture, electronic and optical properties of the synthesized photocatalysts. In the following sections, we discuss the results of several in-depth characterization techniques used to study this phenomenon for some important photocatalysts, i.e., the reference g-C_3N_4 (self-prepared MRref sample and commercially available sample from TCI) and the MR5 sample, as well as the solids MR12 and MR15 as the last representatives of the Simplex optimization method.

3.1. Surface, Chemical, and Textural Analyses. Since the goal of the Simplex optimization method was a larger specific surface area, the first characterization technique applied was the determination of the specific surface area (Table 1) by measuring the nitrogen adsorption−desorption isotherms (Figure 2a) of the selected samples. We can observe from Figure 2a that all investigated photocatalysts exhibit type IV(a) isotherms with H3 hysteresis loops, which indicates a mesoporous structure with slit-like pores.[19−22] The Simplex optimization algorithm enabled us to obtain an atypical DCDA-based high specific surface area g-C_3N_4 by a facile calcination alias a one-step polymerization of the precursor.[23−25] As our initial metric space was adequately predefined, we obtained g-C_3N_4 with a significantly increased specific surface area of 72 m^2/g (MR5 sample) in comparison to the MRref solid (16 m^2/g) and commercially available TCI sample (19 m^2/g). With further calculations, we obtained synthesis parameters that increased the specific surface area of g-C_3N_4 up to 78 m^2/g (MR15 sample) and 86 m^2/g (MR12 solid). The increase of the surface area is, in our opinion, due to the elevated ("harsh") synthesis parameters that lead to the creation of defects and a porous structure of g-C_3N_4, which might originate from increased generation and release of gases during the synthesis.[7,22] In our case, these would probably be CO_2 and NH_3 from the DCDA precursor. However, due to different Simplex calculated synthesis parameters, water vapor might also play a role in the pore formation because of the presence of oxygen and water in the air. For example, when urea was used as a precursor, the generated water vapor increased the porosity of g-C_3N_4.[22] This suggestion is supported by the microporosity of the investigated photocatalysts estimated by the Harkins−Jura theory (*t*-plots in Figure 2c). An increase in the specific surface area of micropores for MR5, MR12, and MR15 samples (10.7, 10.9, and 10.4 m^2/g) in comparison to the MRref (2.17 m^2/g) and TCI (4.5 m^2/g) solids were observed. However, if we compare the microporosity of only MR5, MR12, and MR15 samples, we can find that they express quite similar values since their synthesis conditions are also quite similar. Although MR5, MR12, and MR15 samples were prepared using different temperature ramps and end times, these two factors probably do not play a crucial role in the formation of micropores. However, as already suggested, the high-end temperature in all three cases could improve the micro- and overall porosity of the photocatalysts in comparison to MRref and TCI samples. Especially the mesopores contribute most to the increased specific surface area, as observed from the shape of isotherms in Figure 2a. Figure 2b illustrates the pore size distribution calculated using the Barrett−Joyner−Halenda (BJH) theory, which again shows the more porous structure of MR5, MR12, and MR15 samples compared to MRref, TCI, and four initial g-C_3N_4 (MR1−4) samples. Although medium and larger mesopores (∼12 nm diameter) are abundant, a major increase is observed for the smaller mesopores (∼3 nm diameter). Again, the total- and micropore volume and average pore diameter values of MR5, MR12, and MR15 samples are similar, as were the values of their specific surface areas; thus, no other conclusions could be obtained with this technique.

Table 1. Results of N_2 Physisorption Analysis of the Investigated Photocatalysts (Specific Surface Area, Total Pore Volume, and Average Pore Diameter) and Estimated Microporosity According to Harkins−Jura (Specific Surface Area and Pore Volume)

sample	$S_{BET\ total}$ (m^2/g)	$V_{pore\ total}$ (cm^3/g)	d_{pore} (nm)	$S_{BET\ micropores}$ (m^2/g)	$V_{micropores}$ (cm^3/g)
MRref	16	0.06	18.1	2.2	0.0011
MR1	29	0.006	22.0	-	-
MR2	4	0.02	18.3	-	-
MR3	10	0.04	17.6	-	-
MR4	42	0.15	14.6	-	-
MR5	72	0.24	12.9	10.7	0.0052
MR12	86	0.23	11.2	10.9	0.0050
MR15	78	0.23	11.7	10.4	0.0049
TCI	19	0.09	19.3	4.5	0.0022

The molecular structure of examined solids was further characterized by a combination of IR spectroscopy, ^{13}C and ^{15}N MAS and CP/MAS NMR spectroscopy, and elemental analysis (EA). The FTIR spectra displayed several characteristic features of g-C_3N_4 (Figure 3a). The sharp band at 808 cm^{-1} corresponds to the characteristic breathing mode of triazine or tri-*s*-triazine units of g-C_3N_4 materials.[26,27] The prominent absorption bands at 1204, 1238, and 1316 cm^{-1} are assigned to the C−NH−C unit, while absorption bands in the range between 1600 and 1350 cm^{-1} are due to the vibrations of condensed C−N−C structural units. In particular, the bands at 1311 cm^{-1} belong to the C−N stretching and at 1632 cm^{-1} to the C═N stretching.[28,29] A broad peak centered at 3164 cm^{-1} corresponds to either surface-adsorbed water/hydroxyl functional groups or functional groups still left from the polycondensation (NH_x).[27,28] If we compare the Simplex-optimized g-C_3N_4 samples to those in the MRref solid, we can observe several changes. The broad peak centered at 3164 cm^{-1} is more defined in the case of the MR5 sample and even more so in the case of MR12 and MR15 solids, which indicates a larger content of NH/NH_2 groups in the structure. Peaks at 3084, 3249, and 3280 cm^{-1} probably originate from the N−H stretching vibrations of NH_x groups that were formed during the synthesis. The formed amino groups can be beneficial in improving the charge transfer and photocatalytic performance of g-C_3N_4 as the photocatalyst could become more like a volume photocatalyst.[6,30]

To distinguish whether the synthesized g-C_3N_4 contains triazine or/and tri-*s*-triazine structural motifs in the network, the materials were further investigated by solid-state NMR spectroscopy. The ^{13}C CP/MAS NMR spectra of MRref, MR5, and MR12 samples show a signal at about 157 ppm that is assigned to the carbon atoms of the s-triazine ring ($\underline{C}N_3$) (Figure 3b). Moreover, in the sample MRref, an additional signal appears at 164 ppm assigned to the carbon atoms attached to the amino groups ($\underline{C}N_2(NH_x)$ structural units).[31] Interestingly, the signal at 164 ppm from the MRref sample splits into a peak at 165 ppm and a shoulder at 163 ppm in

https://doi.org/10.1021/acscatal.3c03394
ACS Catal. 2023, 13, 13282−13300

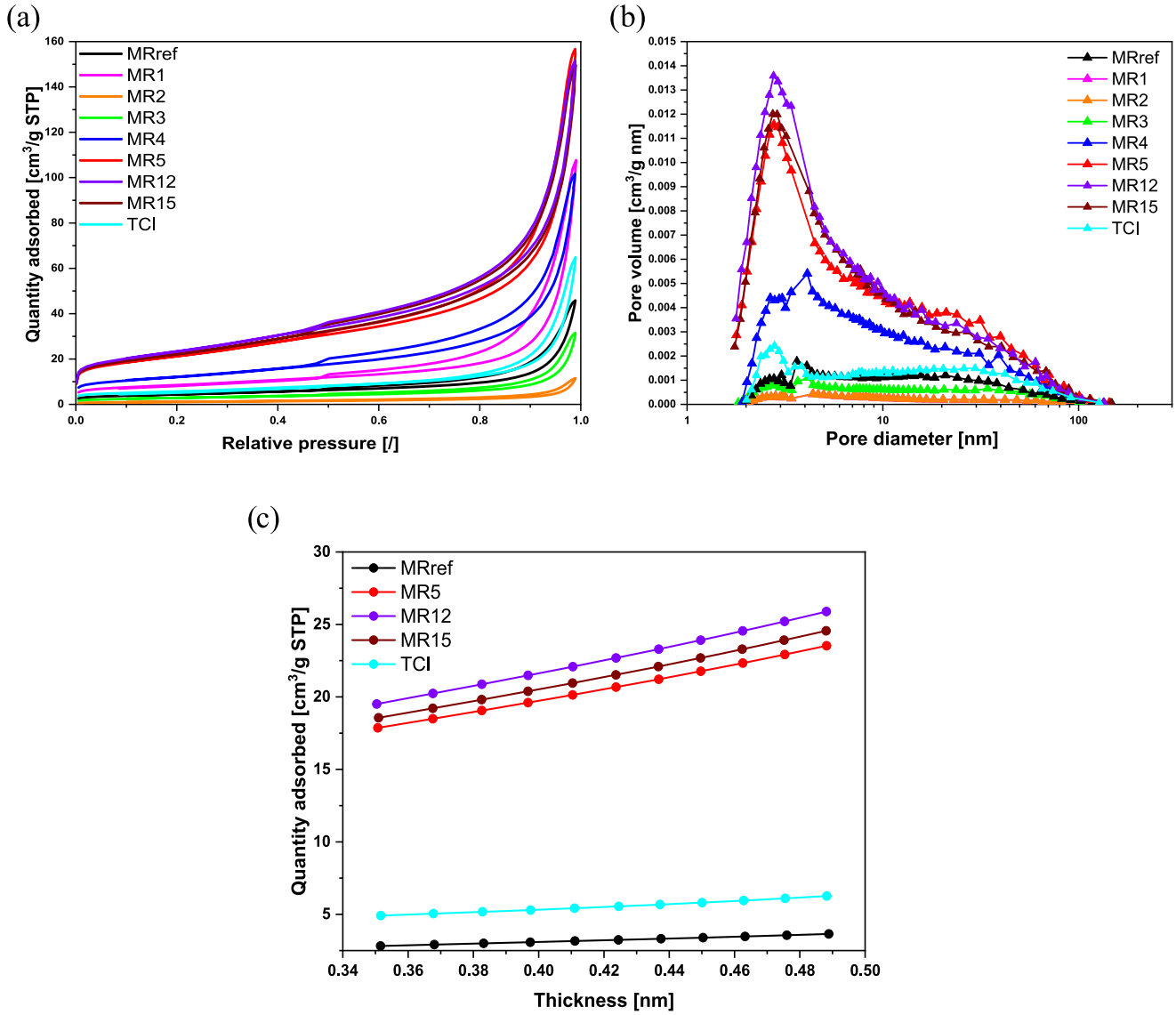

Figure 2. Results of nitrogen physisorption analysis of investigated photocatalysts (starting metric space, two reference materials, and selected three Simplex-optimized photocatalysts): N_2 adsorption−desorption isotherms (a), corresponding BJH pore size distribution (b), and *t*-plots according to the Harkins−Jura thickness equation (c).

samples MR5 and MR12 (Figure 3b,A). To obtain more information about the origin of the latter two peaks, an experiment with direct excitation of the ^{13}C nuclei was performed, and the signal intensities were followed. The cross-polarization was turned off, bypassing the magnetization transfer from the protons to the ^{13}C nuclei, thus making the signal intensities independent of the number of protons in spatial proximity. As depicted in Figure 3b,B, the signal intensities changed compared to the CP-MAS spectrum in Figure 3b,A. The carbon resonances in the s-triazine ring (signal at 157 ppm) gained intensity in samples MR5 and MR12 compared to the signal belonging to the carbon atoms attached to the amino groups (signal at ∼164/165 ppm), while the same intensity was observed in the MRref sample. Thus, the peak at 165 ppm and shoulder at 163 ppm in MR5 and MR12 samples simply indicates a higher population of uncondensed $CN_2(NH_x)$ units in the structure and a different condensation of the g-C_3N_4 network in these samples. We can suggest that our g-C_3N_4 networks consist of tri-*s*-triazine and not triazine building blocks since the signal for the carbon atoms in the triazine structural motif (typically observed in the lower field, i.e., at about 168 ppm) is not seen in our spectra. To further confirm the latter, ^{15}N solid-state NMR spectroscopy was performed. As depicted in Figure 3b,C, three types of signals are found. The peak at about 191 ppm is assigned to the nitrogen ring atoms of the s-triazine ring, while the other two distinct nitrogen peaks at 137 and 110 ppm are assigned to the NH and NH_2 groups, respectively.[31] Although of very low intensity, a signal at 154 ppm can also be seen in the spectra of the MR12 and MR5 samples. This signal belongs to the central nitrogen atom typically found in tri-*s*-triazine, while it does not occur in the structural motif of the triazine. Finally, the elemental analysis reveals the approximate composition of $C_3H_2N_4$ (see Table 2) and C/N molar ratios of 0.67, 0.68, and 0.69 for MRref, MR5, and MR12 samples, respectively. The lower C/N molar ratio compared to that of fully condensed g-C_3N_4 (theoretical ratio of 0.75) confirms the above MAS NMR findings about the presence of a high population of

https://doi.org/10.1021/acscatal.3c03394
ACS Catal. 2023, 13, 13282−13300

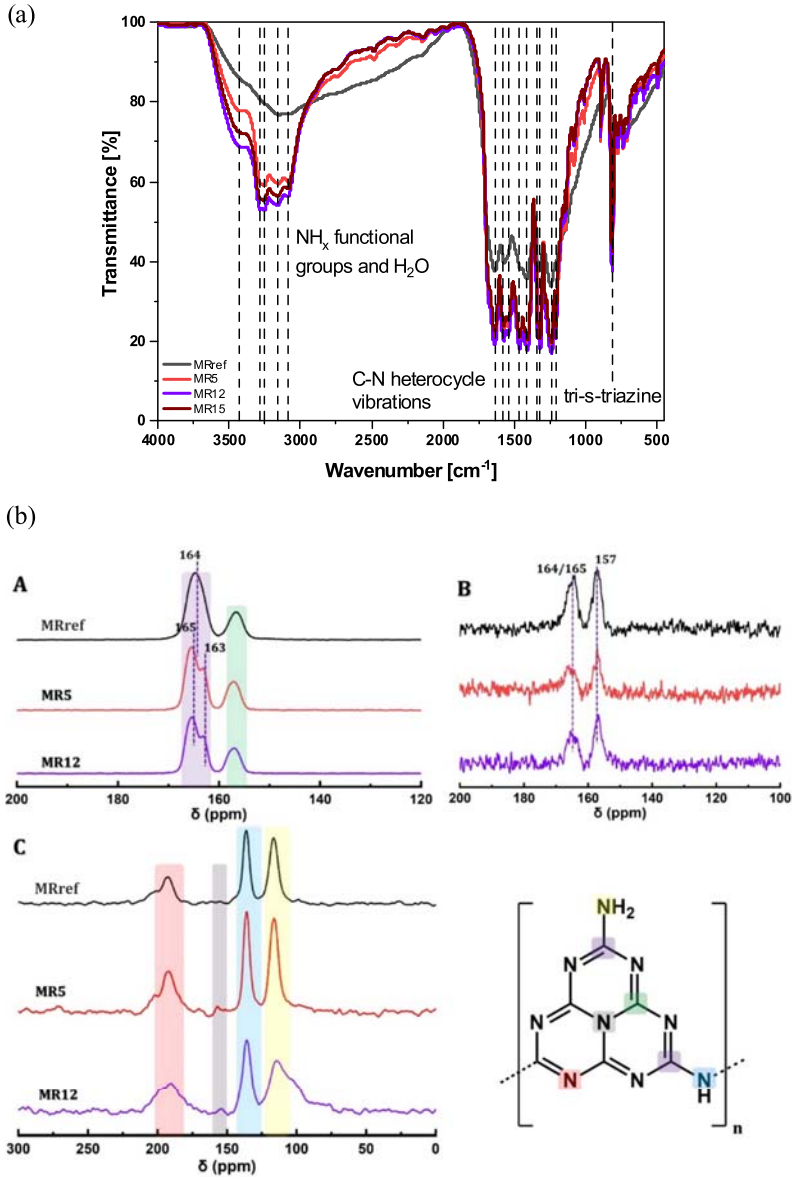

Figure 3. Transmission FTIR measurements (vertical dashed lines represent the characteristic band positions in g-C_3N_4) (a) and results of NMR analysis (b): (A) ^{13}C CP-MAS spectra, (B) MAS NMR spectra, and (C) ^{15}N CP-MAS spectra of MRref, MR5, and MR12 samples with the corresponding tri-*s*-triazine unit scheme.

Table 2. Determination of the Elemental Composition of Fresh Photocatalysts (Carbon, Hydrogen, Nitrogen, and Balance Oxygen and Carbon/Nitrogen Ratio) Employing the CHNS Analysis

sample	C (wt %)	H (wt %)	N (wt %)	O (wt %)	C/N
MRref	34.2	2.0	59.5	4.3	0.67
MR5	35.0	1.8	59.7	3.5	0.68
MR12	34.8	1.9	58.6	4.7	0.69
MR15	34.7	1.8	59.7	3.8	0.68

residual NH groups within or NH_2 groups at the edges of the g-C_3N_4 network of the as-synthesized samples, which is also in agreement with the results of FTIR analysis. All three samples contain significant amounts of H (between 1.80 and 2.06 wt %), suggesting incomplete condensation. Small amounts of oxygen (between 3.5 and 4.7 wt %) detected in the photocatalysts indicate that the materials tend to adsorb water. The highest content of water was detected in the case of the MR12 photocatalyst, which could be favorable as the photooxidation runs are performed in an aqueous medium.

To further confirm the presence and location of NH_x functional groups, we performed Pyr-, CO_2-, and O_2-TPD experiments, the results of which are shown in Figure S4a–d. It can be seen that the concentrations of acidic and basic surface sites and oxygen consumption are minimal (Table S2). This supports the results of FTIR and NMR analyses, which suggested an increased presence of NH_x functional groups in the generated pores between the layers of g-C_3N_4 materials. The access of the probe molecules (Pyr, CO_2, or O_2) to these groups is restricted, thus resulting in the low adsorption observed. Further, these findings are supported by ζ-potential measurements, where the "trapping" of NH_x groups shifted the pH_{PZC} to lower values in comparison to the MRref sample (Figure S4e), as the access to NH_x groups was restricted due to

https://doi.org/10.1021/acscatal.3c03394
ACS Catal. 2023, 13, 13282−13300

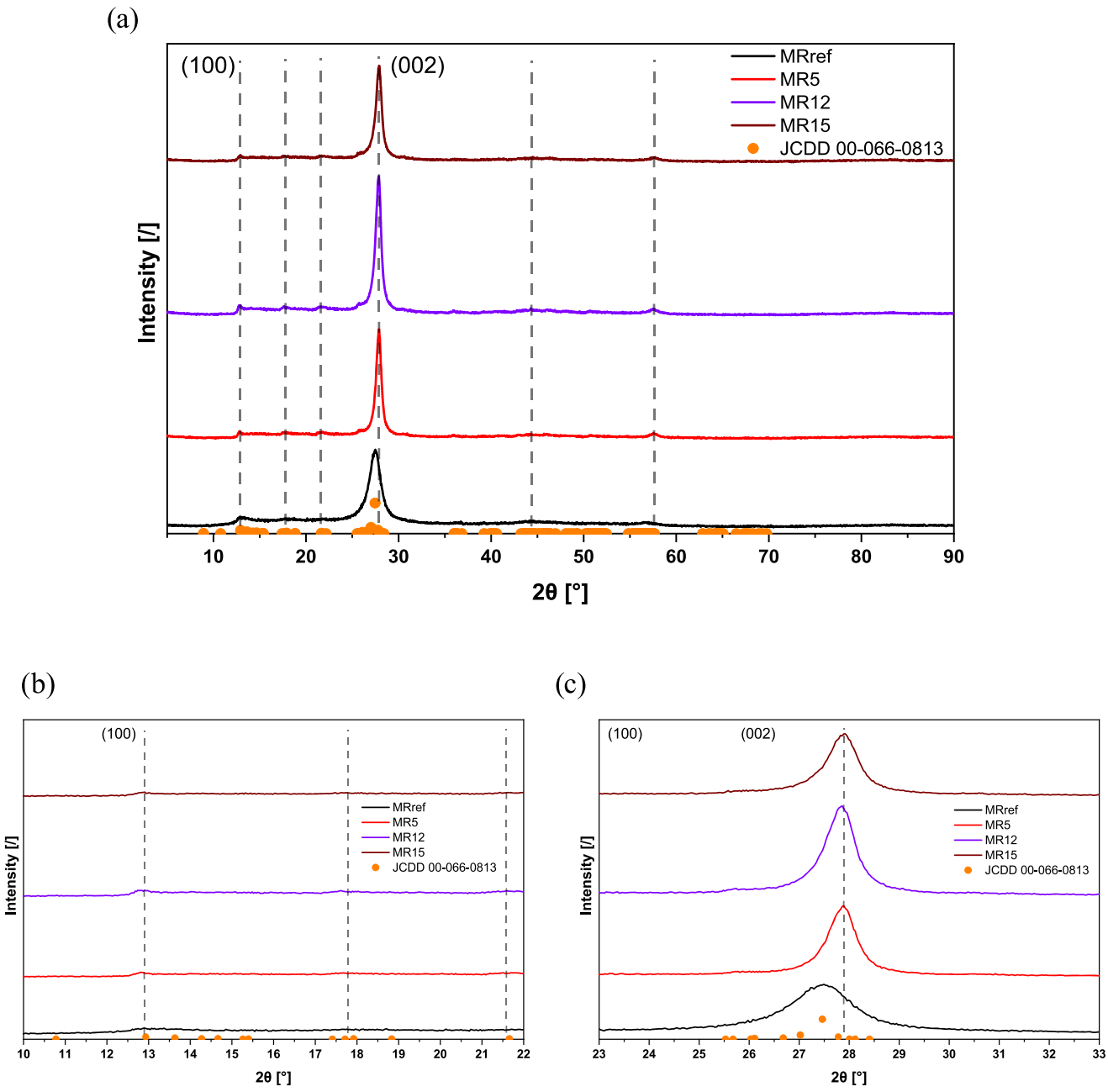

Figure 4. (a) XRD diffractograms of the investigated photocatalysts (vertical dashed lines and orange data points correspond to g-C_3N_4 PDF ICDD 00-066-0813); (b) and (c) show selected peaks from the XRD diffractograms in (a).

ionization.[22] Further information can be found in the Supporting Information.

The phase composition and crystallinity of the investigated photocatalysts were analyzed by powder X-ray diffraction (XRD). The reflection peaks in the XRD patterns correspond to g-C_3N_4, ref ICDD 066-0813 (Figure 4). In all cases, we can observe the presence of the characteristic low-intensity peak (Figure 4b) at around $2\theta = 13°$ that corresponds to the (100) plane of the tri-*s*-triazine unit of g-C_3N_4 and high-intensity peak (Figure 4c) at around $2\theta = 27°$ originating from (002) planes of graphitic materials.[8,29,32,33] From the relative intensity and full width of half-maximum (fwhm) of the (002) peak, we can conclude on low crystallinity of the MRref sample, which is typical for conventional g-C_3N_4 materials synthesized by the polycondensation synthesis.[34,35] In comparison, the MR5 pattern shows a narrower and more intense (002) peak, which indicates more uniform interplanar separation and order,[36] which was already suspected from the results of FTIR analysis (Figure 3a). The MR15 and MR12 samples exhibit even higher intensity peaks for the (002) than for the MR5 or MRref solids. Therefore, the "harsh" synthesis conditions not only improved the specific surface area but also improved the uniform separation of sheets bonded by van der Waals forces.[35,37,38] For example, Cui et al.[35] applied $NaNO_2$ etching to obtain a high crystallinity of g-C_3N_4, which in our case was obtained by just a facile thermal synthesis. An improved crystallinity is favorable as it decreases the charge carrier recombination tendency, which in turn results in an

https://doi.org/10.1021/acscatal.3c03394
ACS Catal. 2023, 13, 13282−13300

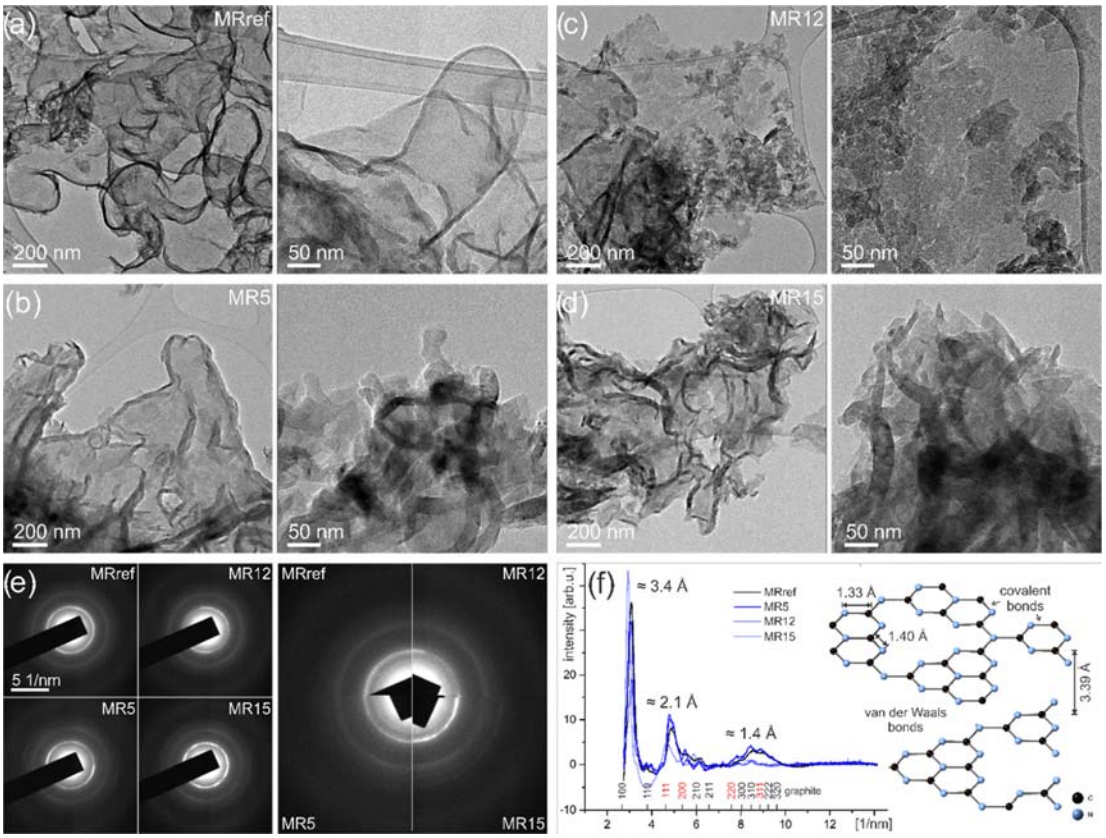

Figure 5. TEM micrographs of MRref (a), MR5 (b), MR12 (c), and MR15 (d) samples with corresponding selective-area electron diffraction (SAED) (e) and image intensity profile derived from rotational-averaged SAED patterns, with the corresponding graphical representation of bond distance (f). Note the large undisturbed sheets of the MRref sample, which for MR5, MR12, and MR15 become more and more segmented, and individual domains become smaller and more voluminous compared to the MRref sample.

improvement of the photoresponse of the material.[39] Table S3 shows that the positions of both peaks for the Simplex obtained photocatalysts shifted to higher 2θ values compared to the MRref sample (Figure 4b,c). Additionally, their *d*-spacing for both peaks slightly decreased, which is advantageous for improved charge carrier transportation and separation, as it makes it easier for the photogenerated electrons to travel through the material, which is an important parameter in photocatalyst design.[40−42] Furthermore, the decreased intralayer distance and narrower width of reflection peaks suggest the presence of thin nanosheets, which is also in agreement with the nitrogen adsorption/desorption experiments.[25] The findings are supported by the TGA measurements performed in the air (Figure S3). The MRref sample exhibits T_{90} and T_{50} values of 595 and 633 °C, respectively, which are lower than the corresponding values for all Simplex-optimized materials. The T_{90} values for MR5, MR12, and MR15 samples are 622, 610, and 622 °C, with T_{50} values of 658, 653, and 654 °C, respectively. This suggests that the Simplex-optimized photocatalysts exhibit improved thermal stability, which can be ascribed to increased van der Waals interactions.

The morphology and texture of the investigated samples were analyzed by TEM (Figure 5). The reference material (MRref) consists of large multilayer sheets, partially overlapping and extending over several micrometers. The rounded edges are ∼20−30 nm thick, corresponding to 5−7 layers. The surface of the individual sheet appears smooth, without any protrusions. A similar size and arrangement of the 2D material can be observed in sample MR5. The individual multilayer sheets are of approximately the same thickness, thickened and often interrupted, and intermixed with scattered individual flaxes of irregular morphologies. In sample MR12, the majority of the sample consists of single-layer foils measuring about 1−1.5 μm^2, intermixed with scarce multilayer sheets of characteristics similar to those in previous samples. The surface of the dominant foils appears torn and segmented, resulting in individual polyhedral crystalline flakes of about 50 nm^2 in size but still assembled in the general form of the original foil. In sample MR15, the majority of the particles are multilayer sheets crushed, forming larger agglomerations. The presence of wrinkles at the edges due to the surface energy minimization and the decreased thickness of materials (especially the MR12 sample) enables the Simplex-optimized materials to exhibit quantum confinement effects that can affect the optical and photocatalytic properties.[40] The crystal structure of the samples was analyzed by selected area electron diffraction (SAED, Figure 5e,f). Similar to XRD analysis, we can detect a small variation in the layer separation (*c*-axis); the MR15 sample deviates the most, approaching the graphene values. Other samples show the same intralayer distances of about 3.4 Å. The more obvious difference between the samples can be observed around 8.5 1/nm, corresponding to intralayer C−N bonds at 1.18 Å. Samples MRref and MR5 show strong scattering from these planes, which indicate smooth, continuous layers. The sample MR12 almost lacks this peak

https://doi.org/10.1021/acscatal.3c03394
ACS Catal. 2023, 13, 13282−13300

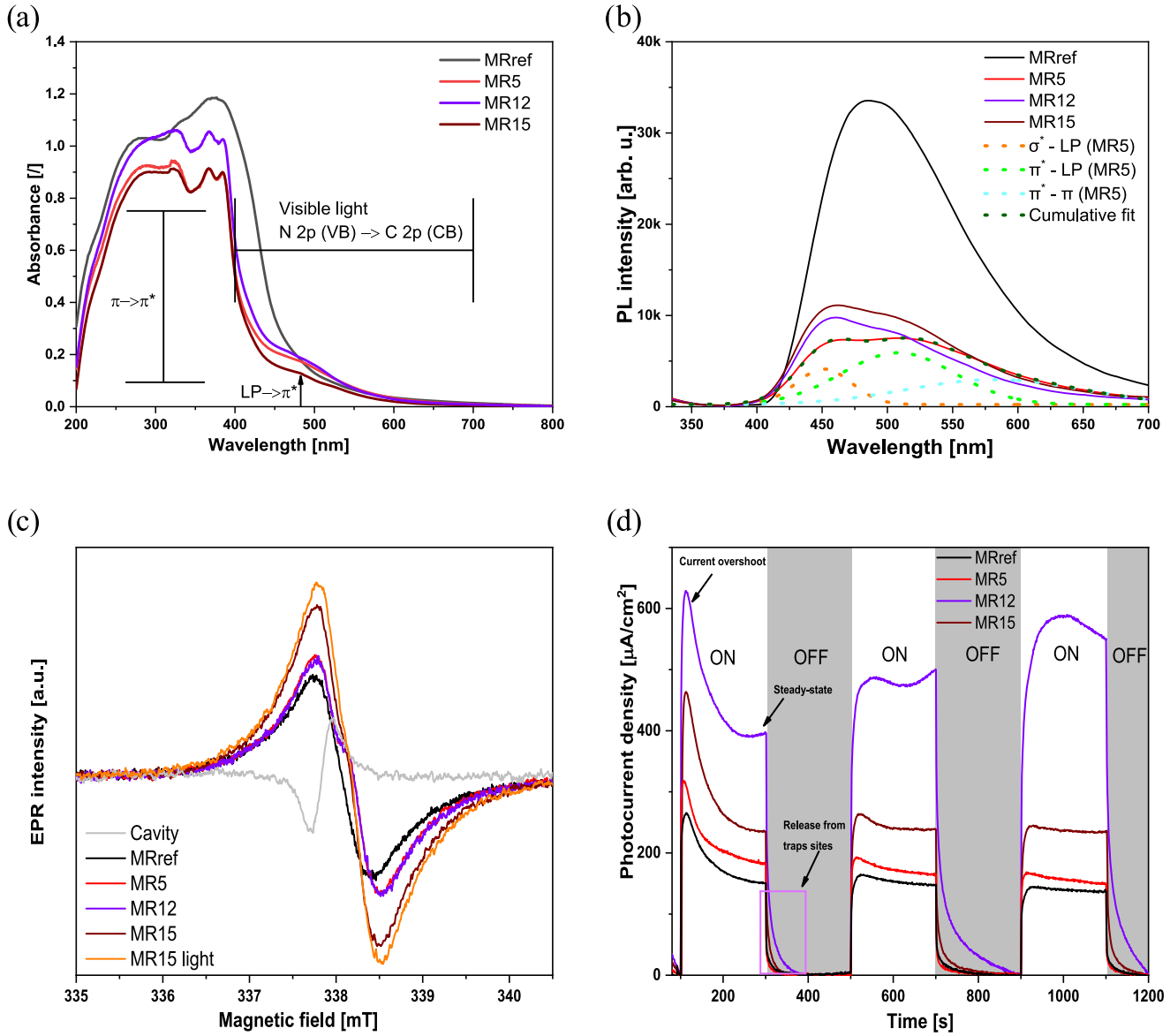

Figure 6. UV−vis-DR (a) and solid-state photoluminescence (PL) spectra (b) of investigated photocatalysts obtained at ambient conditions, solid-state EPR spectra acquired at room temperature (c) and off-on photocurrent density vs time traces (d) obtained under visible-light illumination of the working electrode with deposited catalysts in an aqueous solution of 0.1 M KOH (the release of charge carriers from shallow/deep trap sites is marked with a magenta rectangle).

due to the segmentation of individual sheets on nanoscaled flakes.

Based on the results of XRD and TEM analyses, we define the crystallinity of our g-C_3N_4 samples as the ratio of the crystalline phase contributing to the XRD or electron scattering originating from different crystal planes. The individual monolayers consist of 2D atomic crystals with a nearly orthohexagonal lattice structure, where structural defects alter the bond length of the interatomic valence bond between the atoms forming the basal plane. The monolayers also undergo segmentation, resulting in individual crystalline polyhedral nanoflakes that are further agglomerated, leading to a large number of pores and a larger specific surface area.

The segmentation of the monolayers is reflected in the diffraction peaks originating from the basal plane (a- and *b*-axis). On the other hand, the monolayers are further stacked in the *c*-axis direction and are only weakly bonded by van der Waals forces. The changed stacking of the monolayers, i.e., reduced *d*-spacing, is reflected in the intensity, width, and position of the (002) reflection peak. In our optimal sample, the intralayer distances in the *c*-axis are shortened, so the van der Waals forces are increased compared to the bulk of g-C_3N_4, which improves the thermal stability.

3.2. Determination of Optical and Electronic Properties. UV−vis-DR measurements were performed to determine the light absorption properties of the investigated g-C_3N_4 materials. From the results illustrated in Figure 6a, we can observe that all photocatalysts exhibit visible-light absorption up to 630 nm and intense absorption in the UV region from 280 to 390 nm. The visible-light absorption appears due to the charge transfer of electrons from the valence band (VB) of the N 2p orbital to the conduction band (CB) C 2p orbital.[34] The UV-light absorption is due to the possible $\pi-\pi^*$ transitions in conjugated aromatic systems,[37,43] which seems more defined in

https://doi.org/10.1021/acscatal.3c03394
ACS Catal. 2023, 13, 13282−13300

the case of Simplex-optimized photocatalysts than in the case of the MRref sample (only two broad peaks). The reason for this could originate in the improved crystallinity of samples and the unique surface, chemical, and textural properties discussed above. The absorption edge in all materials behaves like a semiconductor band edge, with a position of ∼468 nm for the MRref sample and ∼429 nm for all Simplex-optimized photocatalysts. The blue shift could occur due to the "harsh" Simplex synthesis conditions that resulted in obtaining nanostructured (thin-layered) g-C_3N_4.

Consequently, the quantum size effects (e.g., quantum confinement effects (QCE)[22,29,44−46]) occur due to the presence of induced quantum states and influence the absorption edge.[2,25,29,35,46] Simultaneously, the generated micropores, as observed from the results of NMR, FTIR, BET analyses, and TPD experiments, where the presence of NH_x functional groups in the layered structure of Simplex-optimized g-C_3N_4 was suggested, destroy the π-conjugation and the range of π-conjugation; thus, a blue shift occurred as the absorption edge corresponds to the $\pi-\pi^*$ transitions.

For example, Liu et al.[47] used the functional groups present in pores of 2D hexagonal boron nitride (h-BN) to form B−O−Ti bonds. As the h-BN is a similar planar system like g-C_3N_4, we can tentatively assume that the detected NH_x functional groups are also at least partly present inside the pores as well as trapped in the layers of g-C_3N_4 according to our TPD experiments.[48] An additional broad peak appeared for all Simplex-optimized photocatalysts centered at around 480 nm (Figure 6a), which can be ascribed to the presence of nitrogen vacancies and/or intrinsic electronic transitions (LP-π^*).[25,37,43] These double electron transitions occur when defects and/or distortions are present in the structure, as in an ideal planar structure of a polymer, and the LP-π^* transitions are forbidden.[37,43] Using the pure absorption measurements (i.e., excluding scattering; Figure S5a), we determined that the blue shift and the presence of the second peak is a property of the material that does not occur due to scattering. The deviation of the ideal planar structure was observed in the TEM images (Figure 5), especially in the case of the MR12 photocatalyst that forms ordered nanoflakes of thin g-C_3N_4 foils, where the additional presence of NH_x functional groups formed distortions due to the formation of −NH− bonds in the interchain.[37] This was observed in the TEM analysis with the wrinkling of the nanosheets. Therefore, the presence of the double transitions in all Simplex-optimized materials and their absence in the case of the MRref sample tentatively confirm the presence of defects, probably in the form of generated micropores and the formed nanoflakes that are different from the nanosheets in terms of our definition of crystallinity and defects.

Using the Kubelka−Munk theory (eq 1),[37] we estimated the optical band gap (E_g^{opt}) values of the investigated photocatalysts as follows:

$$(\alpha h\nu)^2 = A(h\nu - E_g^{opt}) \quad (1)$$

where α, $h\nu$, E_g^{opt}, and A are absorption coefficient, photon energy, direct (optical) band gap, and proportional constant, respectively. Therefore, the E_g^{opt} values are 2.63, 2.96, 2.94, and 2.95 eV (Table 3) for MRref, MR5, MR12, and MR15 samples, respectively. Interestingly, the E_g^{opt} values of the Simplex-optimized g-C_3N_4 samples are blue-shifted, which can be advantageous, as higher band gap values limit the charge carrier recombination. The origin of this phenomenon can be attributed to the fact that the conduction and valence bands shift in opposite directions when the thickness of g-C_3N_4 is reduced and the QCE are present, as observed by Zhang et al.[49] in their theoretical and experimental research.

Table 3. Determined Conduction (CB) and Valence (VB) Bands vs NHE, Calculated Highest Occupied Molecular Orbital (HOMO) and Lowest Unoccupied Molecular Orbital (LUMO) Positions, Calculated Optical (E_g^{opt}) and Electrochemical (E_g^{el}) Band Gap Values, and Comparison of Charge Transfer Resistance (R_{CT}) of Investigated Photocatalysts

sample	CB vs NHE (V)	VB vs NHE (V)	HOMO (V)	LUMO (V)	E_g^{el} (eV)	E_g^{opt} (eV)	R_{CT} (MΩ)
MRref	−0.89	1.75	3.27	5.91	2.64	2.63	4.46
MR5	−0.91	1.75	3.25	5.91	2.66	2.96	3.07
MR12	−0.94	1.75	3.22	5.91	2.69	2.95	2.66
MR15	−0.92	1.73	3.24	5.89	2.65	2.94	2.83

To obtain information on the edge potentials of examined photocatalysts, we performed cyclic voltammetry (CV) measurements (Figure S5b). All cyclic voltammograms have a quasi-rectangular shape that indicates pseudocapacitive characteristics.[50] Due to the presence of different positions of nitrogen atoms in the g-C_3N_4 structure, the voltammograms are more complex.[51] All investigated photocatalysts exhibit similarly enclosed areas, which suggests that no changes occurred concerning their capacitive behavior. The oxidation potential (E_{ox}) and reduction potential (E_{red}) onset were obtained from Figure S5b and are presented in Table 3. The potentials are typically correlated to the valence (VB) and conduction (CB) bands of photocatalysts. For conversion between the potential (E) of SCE and NHE, we used eq 2

$$E_{NHE} = E_{SCE} + 0.24 \quad (2)$$

From the results listed in Table 3, we can observe that the VB and CB potentials are similar in all investigated photocatalysts, as their chemical compositions are also similar. The determined edge potential of the CB for all photocatalysts is more negative than the reduction potential of oxygen (−0.046 eV vs NHE[52,53]); thus, photogenerated e^- in all photocatalysts can react with water-dissolved oxygen to generate $O_2^{-\bullet}$. The potential for the $OH^\bullet/H_2O$ (2.68 eV vs NHE) and $OH^\bullet/OH^-$ (1.99 vs NHE)[53] is too positive for the photogenerated h^+ in the VB of all photocatalysts to produce $OH^\bullet$ radicals. The difference between these two potentials represents the electrochemical band gaps (E_g^{el}). As can be observed from the results listed in Table 3, the values of E_g^{el} and E_g^{opt} are different. The reason for the larger E_g^{opt} in comparison to the E_g^{el} is probably the effect of (i) morphology and quantum confinement and (ii) the effect of the solvent, temperature, and electrolyte.[54,55] In particular, the morphology and quantum confinement effect explain the increased (∼0.32 eV) E_g^{opt} in all Simplex-optimized photocatalysts in comparison to the E_g^{opt} of the MRref sample. In the case of electrochemical determination, these two effects do not play a crucial role, and the E_g^{el} values are more in the expected (moderate) range. However, a slight increase in E_g^{el} values in all Simplex-optimized materials is observed. Using eqs 3 and 4, we calculated the corresponding profiles of frontier orbitals HOMO (IP) and LUMO (EA) for investigated photocatalysts and listed them in Table 3:[56]

https://doi.org/10.1021/acscatal.3c03394
ACS Catal. 2023, 13, 13282−13300

$$\mathrm{IP} = E_{\mathrm{ox}} + 4.4 \quad (3)$$

$$\mathrm{EA} = \mathrm{IP} - E_{\mathrm{g}}^{\mathrm{el}} \quad (4)$$

To investigate the charge carrier recombination tendency, we performed the solid-state photoluminescence (PL) measurements, where we measured the radiative charge carrier recombination.[57] From the PL spectra depicted in Figure 6b, we can observe a broad PL signal with a maximum at around 485 nm for the MRref sample. For MR5, MR12, and MR15 solids, we can distinguish two peaks at around 460 and 507 nm, which is especially expressed in Figure S5c, where the illustrated data were recorded using a wider emission slit (set to 1 nm). This is due to the before-mentioned QCE.[46] In Figure 6b, the solid PL spectra for g-C_3N_4 contained three different transitions: σ^*-LP, π^*-LP, and $\pi^*-\pi$.[58−60] Therefore, we performed a deconvolution of the PL spectra using a three-peak Gaussian fit model (Figure S6). Peak 1 at around 450 nm corresponds to σ^*-LP transitions, peak 2 at around 500 nm to π^*-LP transitions, and peak 3 at around 570 nm to $\pi^*-\pi$ transitions.[58,60] Interestingly, for the Simplex-optimized materials, we can observe the presence of peak 1 and some indication of peak 2 (Figures 6b and S5c). In the MRref material, all three peaks are combined in a single broad signal. As the MR5, MR12, and MR15 samples exhibit a more nanosized and crystalline structure, quantum size effects occur, which can be reflected in different optical and electronic properties. If we compare the peak positions, no major changes are observed, except for a slight blue shift that occurred in all Simplex-optimized photocatalysts. This is in agreement with the results of UV−vis-DR, TEM, and FTIR/NMR analyses as a PL blue shift occurs due to the presence of pores in the plane and crumbled structure (nanoflakes) that enables the presence of QCE and opposite shifting of the CB and VB of the materials.[61] However, the intensities (peak areas) change for the investigated materials (Table S4). The improvement of the structural characteristics can be observed by a decrease in PL intensity for all Simplex-optimized photocatalysts. The lower heating ramp, in comparison to the MRref sample, and the longer synthesis duration induced the generation of defects in the structure that especially affected the nitrogen atoms with the generation of NH_x functional groups, which hindered the charge carrier recombination.[62] Kang et al.[63] proposed that the tricoordinated N atoms are absent from the VB and CB edges; thus, they are localized and promote charge carrier recombination in bulk g-C_3N_4. Therefore, if these N atoms are forced to undergo changes in NH_x functional groups inside the material, as observed by the FTIR, NMR, and nitrogen adsorption/desorption experiments, the charge carrier recombination tendency decreases, as observed in Figure 6b.

In the deconvoluted spectra (Figure S6), the MR5 sample expressed the most decreased area for all three transitions in comparison to the MRref sample. In the case of the MR12 sample, only peak 1 area increased in comparison to the MR5 sample, although the areas for transitions π^*-LP and $\pi^*-\pi$ decreased. Structural differences between MR5 and MR12 samples were already observed, which affected the electron transitions. For example, structural defects can act as traps, which slow down or even hinder the radiative recombination of charge carriers. However, a too-large content of defects has a negative effect, as they can act as recombination centers.[64] This is observed in the case of the MR15 sample, which exhibits the highest charge carrier recombination among all Simplex photocatalysts, which could be due to slightly lower crystallinity (XRD and TEM analysis) and the possible high amount of structural imperfections.[40] However, charge carriers can recombine with different nonradiative mechanisms that affect the charge carrier dynamics.

To gain further insight into the electronic/structural properties of the investigated photocatalysts, we first performed the solid-state EPR measurements at room temperature (Figure 6c). It can be seen that the EPR spectra of the studied materials consist of a single Lorentzian line, as can be observed when comparing the experimental spectra with the simulated spectra (Figure S7a). The *g*-value of most samples corresponded to the value of 2.004, although the range is from 2.009 to 2.003 due to some minor variations in the working frequency of the EPR spectrometer.[40,41] However, the *g*-values in all cases can be attributed to the unpaired electron in the g-C_3N_4 π-network at the sp^2 atom.[29,40] We can further observe in Figure 6c that all Simplex-optimized photocatalysts exhibit a higher EPR signal in the dark than the MRref sample, thus possibly containing a higher number of defects. Interestingly, the highest EPR signal, thus the sample with the potentially highest content of structural defects (trap states[45]), is MR15 solid, as these defects can act as paramagnetic centers.[29] Structural defects (e.g., nitrogen vacancies,[42] defects in the layers or structure, distortions, etc.) can reduce crystallinity, which was observed in the case of the MR15 sample, as it had lower crystallinity, by our definition, than the MR12 photocatalyst (Figures 4 and 5). Additionally, a too-high number of defects can act as recombination centers, as seen in the PL spectra for the MR15 sample (Figure 6b).[42] In Figure 6c, we can also observe that under visible-light illumination, the EPR intensity increases, as demonstrated for the MR15 photocatalyst, where the photogenerated electrons are trapped due to the presence of defects.[29] This phenomenon is seen more clearly in Figure S7b, where the *in situ*, time-resolved measurements are represented at the temperature of liquid nitrogen for the MR12 sample. It can be observed that the generated electrons are trapped at the defect sites as their intensity increases from $t = 0$ min (scan starts immediately after light source ON) up to $t =$ 15 min and then remains almost the same up to $t = 45$ min. As e^- is trapped, it can accumulate and provide the observed increase in EPR intensity. Using EPR analysis, we therefore confirmed conclusions derived from the results of structural (BET, FTIR, NMR, TPD) as well as UV−vis-DR and PL analyses about the presence of defects, which were probably in the form of pores created with the "burning" of the trapped DCDA precursor and/or holes in the infinite 2D layer of g-C_3N_4.

To complement the results of PL and EPR analyses, we further performed EIS (Figure S8), photoresponse (Figure 6d), and TCSPC measurements (Figure S9) as well as phosphorescence decay and QY analyses (Figure S11a,b). The MR12 photocatalyst exhibits the lowest charge transfer resistance (R_{CT}) value of 2.66 MΩ and the highest photocurrent with the longest relaxation duration, which is due to the improved crystallinity, lower thickness of layers, and "trapped" NH_x functional groups in pores.[8,44,65,66] The average photoluminescence lifetime of charge carriers was also found to be the highest for the MR12 sample (Figure S10b) at the emission peak of 490 nm (12.7 ns, Table S4). The long lifetime of the charge carriers and their increased mobility could be attributed to the nanostructure observed in TEM

https://doi.org/10.1021/acscatal.3c03394
ACS Catal. 2023, 13, 13282−13300

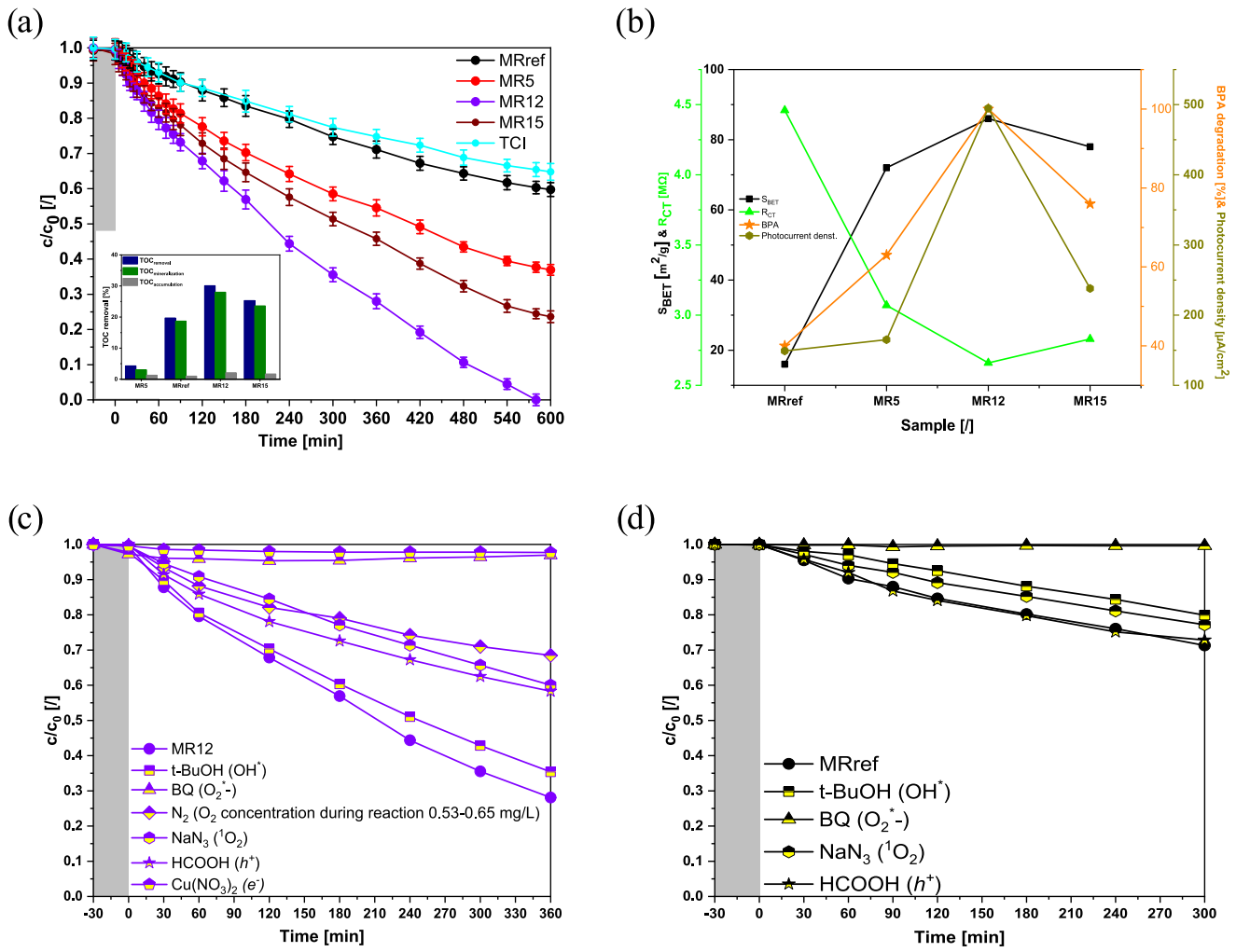

Figure 7. Photocatalytic oxidation of water-dissolved BPA in the presence of investigated photocatalysts under visible-light illumination (inset represents the values of total organic carbon (TOC) removal at the end of BPA degradation runs) (a) and correlation between BPA degradation and the properties of investigated photocatalysts (b). (c) and (d) represent *in situ* quenching experiments of BPA photooxidation for MR12 (c) and MRref (d) samples under visible-light illumination. The gray area in the graphs represents the visible-light-off period.

(Figure 5), which influences (enhances) the diffusion path of the free charge carriers. In addition, the nanostructure affects the mass transfer and access to the active sites in the photocatalyst. The presence of residual functional groups observed by FTIR, NMR, and EPR techniques further enhances the charge carrier mobility due to the changes in the electronic structure of g-C_3N_4 (presence of carbon sites) and the presence of NH_x functional groups.[67] This again implies that the photogenerated carriers can be utilized for redox reactions for a longer period of time, leading to improved properties of the MR12 photocatalyst in comparison to the MRref sample, which is due to the Simplex-optimized synthesis parameters. For further details, refer to the Supporting Information.

3.3. Photocatalytic Oxidation and Determination of Reactive Oxygen Species. To evaluate the applicability of the synthesized photocatalysts for the heterogeneous photocatalytic wastewater remediation, we performed the photooxidation of an aqueous solution of bisphenol A (BPA) under visible-light illumination. Of all of the bisphenols, bisphenol A (BPA) is most commonly used in packaging materials that end up in landfills. Rain, snow, and other environmental factors cause BPA to leach into the soil and contaminate underground drinking water reservoirs.[68] This is a major concern because BPA is considered an endocrine disruptor that interferes with estrogens in the developing human brain.[69]

From the results illustrated in Figure 7a, we can observe that all investigated photocatalysts exhibit the ability to degrade BPA. As expected, due to its low specific surface area and poor structural and electronic properties, the MRref sample exhibits a low BPA degradation rate (39.6% in 600 min of irradiation), which is similar to the degradation rate of the commercially available g-C_3N_4 sample (TCI). In comparison, all Simplex-optimized g-C_3N_4 solids exhibit improved BPA oxidation, which is in agreement with the outcome of the performed characterization. The most active photocatalyst enabling complete BPA degradation in the given range of operating and reaction conditions is the MR12 photocatalyst (100% BPA conversion after 580 min of visible-light illumination), followed by MR15 and MR5 samples (BPA conversion of 76.4 and 62.7%, respectively, after 600 min of visible-light illumination). The origin of the high activity of the MR12 photocatalyst lies in the optimal balance between crystallinity, specific surface area, and electronic properties, which enables the optimal

https://doi.org/10.1021/acscatal.3c03394
ACS Catal. 2023, 13, 13282−13300

utilization of generated charge carriers (Figure 7b). This means that we did not only optimize the specific surface area using the Simplex method but also other important factors like charge carrier mobility. The inset in Figure 7a shows that the synthesized photocatalysts exhibit a high degree of mineralization, with only a minor accumulation of surface carbon during the BPA degradation run. Moreover, assuming the pseudo-first-order kinetics (Figure S12a), we calculated the values of reaction rate constants using eq 5

$$\ln\left(\frac{c_0}{c_t}\right) = kt \tag{5}$$

where c_0 is the initial BPA concentration, c_t is the actual BPA concentration at a selected time, k is the photodegradation reaction rate constant, and t is the selected time.[5] The corresponding reaction rate constants are 1.13×10^3, 2.44×10^3, 4.44×10^3, and 3.33×10^3 min^{-1} for MRref, MR5, MR12, and MR15 samples, respectively. As expected, the MR12 photocatalyst exhibits the highest initial BPA degradation rate. The optimal synthesis procedure obtained by the Simplex method did not only improve the characteristics of the MR12 sample (specific surface area, electronic properties) for enhanced photocatalytic activity but also provided high stability g-C_3N_4 photocatalyst, as was already suggested by the results of TGA analysis (Figure S3). Consequently, the same batch of the MR12 photocatalyst was tested in five reusability cycles (Figure S12b), where the drop in the photocatalytic activity was slight (~9%).

To understand the very first reaction steps of BPA degradation (i.e., the involvement of active species), we performed *in situ* quenching experiments with the MR12 and MRref photocatalysts under visible-light illumination for 360 min. For this purpose, the following scavengers were employed: *t*-BuOH ($OH^\bullet$), BQ ($O_2^{-\bullet}$), purging with N_2 (removal of water-dissolved O_2), NaN_3 ($^1O_2$), HCOOH (h^+), and $Cu(NO_3)_2$ (e^-). From Figure 7c, it can be observed for the MR12 photocatalyst that adding *t*-BuOH only minimally decreased the photocatalytic activity. This was expected due to its unfavorable VB position (Table 3), which is not suitable for forming $OH^\bullet$ radicals directly. On the other hand, the addition of either BQ or $Cu(NO_3)_2$ nearly completely decreased the photocatalytic degradation rate of BPA, as photogenerated e^- are needed to form $O_2^{-\bullet}$, which is a crucial ROS when g-C_3N_4 is used.[5] Another interesting trend was observed with the addition of NaN_3 and HCOOH, as they both inhibited the photocatalytic activity of the tested materials by around 50%. This was expected as the materials that are similar to organic macromolecules produce $^1O_2$.[70,71] In large organic macromolecules and materials such as organic macromolecules, the $^1O_2$ can, in theory, be generated via three different pathways. However, the generation typically occurs with either or both chemical reaction generation or physical generation (energy transfer).[71] The chemical generation of $^1O_2$ can occur with two typical reactions, either between h^+ and $O_2^{-\bullet}$ or $O_2^{-\bullet}$ and H_2O.[72] Another possibility for the generation of $^1O_2$ is exciton energy transfer, in which energy is transferred from the excited photocatalyst to $^3O_2$.[73−75] In that case, the photocatalyst behaves similarly to larger carbon-containing macromolecules (i.e., Rose Bengal).[76] The differentiation between the energy transfer mechanism and chemical generation of $^1O_2$ is difficult, as typically both processes take place, and the longevity of the species is reduced in the aqueous medium.

To determine the most probable generation mechanism, we need to look at *in*-situ quenching experiments. As both quenching experiments for h^+ and $^1O_2$ have similar BPA degradation rates, we suspect that the h^+ reacts with $O_2^{-\bullet}$ according to eq 6 to form $^1O_2$.[77,78] However, from Figure S11a, we can observe that the MR12 photocatalyst exhibits a phosphorescence decay; thus, the energy transfer mechanism could be possible.[70]

$$O_2^{-\bullet} + h^+ \rightarrow {}^1_aO_2 \tag{6}$$

However, quenching with BQ that acts as an $O_2^{-\bullet}$ scavenger gives more information on the dominant mechanism. In our case, water-dissolved O_2 and e^- were still present in the BPA/photocatalyst suspension when BQ was added. This means that $^1O_2$ could theoretically be formed by the energy transfer. However, with the addition of BQ, the photocatalytic degradation decreases nearly completely and is different than in the case when NaN_3 was used as a $^1O_2$ scavenger, meaning that $^1O_2$ is either formed from $O_2^{-\bullet}$ and H_2O or $O_2^{-\bullet}$and h^+.[72,77,78] As the quenching experiments for h^+ and $^1O_2$ gave similar results, we assumed that the generation of $^1O_2$ occurred predominantly with the reaction described in eq 6.[70] Nevertheless, the energy transfer cannot be completely discarded because it could also be enhanced with the observed presence of QCE in the Simplex-optimized samples as they influence the energy states and transitions in organic materials.[2,71,76,79,80]

As the quenching with NaN_3 or HCOOH did not completely stop the photooxidation, this probably means that not all $O_2^{-\bullet}$ is converted to $^1O_2$ and both $O_2^{-\bullet}$ and $^1O_2$ are the responsible active ROS for the degradation of BPA. Because the MR12 photocatalyst produces $O_2^{-\bullet}$ and $^1O_2$, it acts simultaneously as a Type I and Type II ROS photosensitizer,[81,82] which usually requires organometallic complexes, usage of plasmonic metals on different supports,[75] or large organic macromolecules.[76] Moreover, the generation of singlet oxygen is generated probably with the dismutation reaction, hole oxidation, and energy transfer as observed in ref 70 and our experiments.

The production of $^1O_2$ is also in agreement with the results of the reusability and TGA experiments, as it is typical that materials capable of producing $^1O_2$ show high stability.[75] We additionally performed BPA degradation experiments by purging the reaction suspension with N_2 (end O_2 concentration 0.56−0.65 mg/L), which resulted in a similar BPA degradation rate as during the experiments where NaN_3 and HCOOH were employed. We assume that some surface-adsorbed oxygen was left that could participate in the generation of ROS. In addition, the h^+ present could attack the surface-adsorbed BPA molecules directly, as nearly no oxygen was available to form $O_2^{-\bullet}$ that would react with h^+ to form $^1O_2$. It can be concluded that the photogenerated h^+ can degrade the surface-adsorbed BPA if no water-dissolved oxygen is present and plays a key role in the generation of ROS ($^1O_2$) in the presence of oxygen.

Interestingly, when we performed the quenching experiments in the presence of the MRref sample, the determined reactive oxygen species was $O_2^{-\bullet}$ since the photooxidation rate of BPA was reduced only to a low extent by the addition of NaN_3 and *t*-BuOH. The generated h^+ probably could not play an important role, as the specific surface area of the MRref

https://doi.org/10.1021/acscatal.3c03394
ACS Catal. 2023, 13, 13282−13300

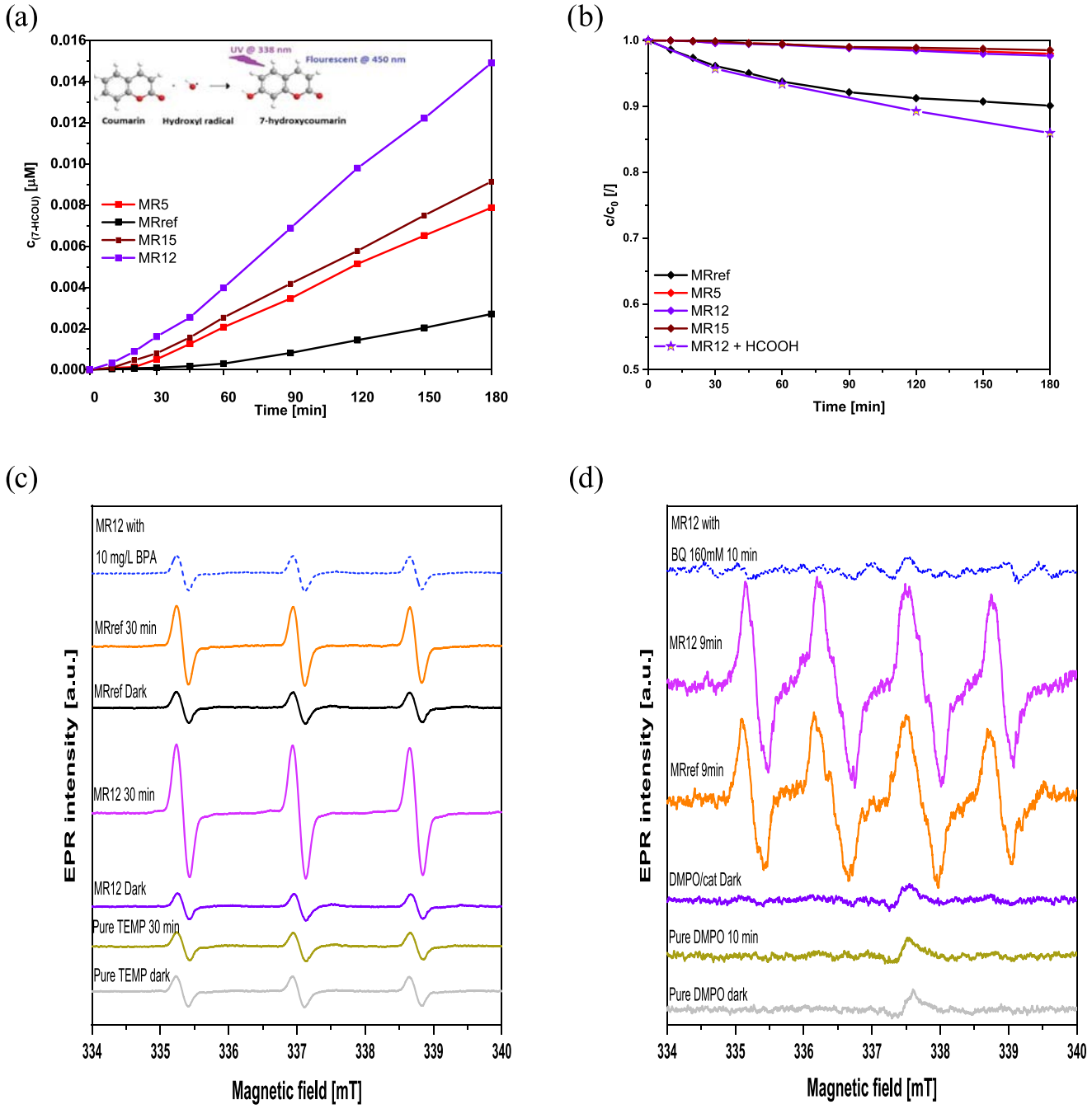

Figure 8. Dependence of 7-hydroxycoumarin (a) and relative $ABTS^{\bullet+}$ (b) concentration on irradiation time measured upon visible-light exposure (Schott, model KL 2500 LED) for investigated materials, EPR spin trap measurements of water-dissolved TEMP (c) and DMPO in DMSO (d) in the presence of MRref and MR12 photocatalysts under different experimental setups.

sample is low, which limits the access of water-dissolved species to the active sites. These trends can be ascribed to the absence of the quantum confinement effect, as the MRref sample presents a thicker layered material in comparison with the MR12 solid (Figure 5). Additionally, the MR12 photocatalyst expressed a higher content of oxygen than the MRref sample (Table 2), which favors the generation of $^1O_2$.[82] The results show that by using the Simplex optimization method, we can not only optimize g-C_3N_4 but also manipulate the generation of different types of ROS.

We further studied the photooxidation of different emerging bisphenols[83] using the MR12 photocatalyst under visible-light illumination. From Figure S13a, it can be observed that the more stable BPA analogues exhibited a lower photooxidation rate than BPA; however, due to the generation of $^1O_2$, the degradation of BPAF and BPS was unexpectedly high.[65] Moreover, under simulated solar irradiation (Figure S13c), the degradation of BPA, BPAF, and BPS significantly increased due to the presence of UV emissions in addition to the increased lamp intensity (1 Sun), which proves the possibility of real-life application of the MR12 photocatalyst. The generated $^1O_2$ additionally exhibited a selective oxidation potential when different pharmaceutical compounds were treated (Figure S13b). Only caffeine, paracetamol, and salicylic

https://doi.org/10.1021/acscatal.3c03394
ACS Catal. 2023, 13, 13282−13300

acid were degraded under visible-light illumination, which prevents the formation of toxic byproducts, for example, that are generated when benzoic acid is oxidized.[72,84] Furthermore, due to the generation of $^1O_2$, the application possibilities of the MR12 photocatalyst increased to water remediation using solar irradiation (Figure S13c), organic synthesis,[82,85] detoxification, and decontamination processes.[75] For further information, refer to the Supporting Information.

3.4. Mechanistic Study of Reactive Oxygen Species under Visible-Light Illumination. The generation of different ROS was further confirmed by performing EPR measurements in the liquid phase using TEMP ($^1O_2$) and DMPO ($O_2^{-\bullet}$ or $OH^\bullet$) traps under various experimental conditions. As can be observed in Figure 8c, pure TEMP under visible-light illumination and TEMP/catalyst suspension in the dark do not produce the TEMP−$^1O_2$ adduct, as the signal intensity is the same as for the pure TEMP in dark conditions. When the suspension containing MR12 or MRref photocatalyst is illuminated, the signal of the TEMP−$^1O_2$ adduct (1:1:1 triplet signal) increases, proving the generation of $^1O_2$. As was already observed in the BPA quenching experiments (Figure 7c,d), the MR12 photocatalyst produces $^1O_2$ in a higher amount than the MRref sample, thus showing that $^1O_2$ is one of the crucial ROS. These findings are confirmed in Figure 8c, where the signal increase in the case of the MR12 photocatalyst is significantly larger than in the case of the MRref sample. This was expected due to the thin-layered structure of the MR12 photocatalyst that enabled quantum confinement effects and improved charge carrier transfer properties. To demonstrate that the degradation of BPA occurs with $^1O_2$, we prepared the TEMP solution with BPA (initial concentration of 10 mg/L). It can be seen in Figure 8c that the signal for the TEMP−$^1O_2$ adduct does not increase for the MR12 photocatalyst as it did when no BPA was present in the reaction mixture. This means that $^1O_2$ has a higher affinity to attack BPA (0.0438 mM) than the abundant TEMP (7.08 mM) and proves that $^1O_2$ can react with BPA.

To confirm the generation of $O_2^{-\bullet}$, DMPO dissolved in DMSO was used to stabilize the DMPO-$O_2^{-\bullet}$ adduct. Again, as can be observed in Figure 8d, both pure DMPO under visible-light illumination and DMPO/catalyst suspension in the dark do not produce the characteristic signals of the DMPO-$O_2^{-\bullet}$ adduct (1:1:1:1 quartet). Under visible-light illumination, MRref and MR12 photocatalysts produced $O_2^{-\bullet}$ as the DMPO-$O_2^{-\bullet}$ adduct was formed. Additionally, the broadness of the peaks can be ascribed to the DMPO-OCH_3 adduct formed by the reaction with the solvent (DMSO) under visible-light illumination[86] or to the interactions of O_2 with DMPO-$O_2^{-\bullet}$,[87] as the photocatalysts contain small amounts of oxygen. In the case of the MR12 sample, the signal intensity of the DMPO-$O_2^{-\bullet}$ adduct was increased in comparison to the MRref solid due to the above-mentioned improvements of properties of the MR12 sample. The addition of BQ inhibits the generation of the DMPO-$O_2^{-\bullet}$ adduct, thus proving that the signal originated from the $O_2^{-\bullet}$. Furthermore, we purged the DMPO/DMSO/MR12 suspension with different gases before illumination (Figure S14a). When we purged the suspension with N_2 or He, the DMPO-$O_2^{-\bullet}$ adduct was still formed, although with a minor decrease. The reason could be that the MR12 photocatalyst contains a large amount of adsorbed oxygen (~5%, Table 2). As the photocatalyst was not degassed, the present oxygen could still form $O_2^{-\bullet}$; thus, the DMPO-$O_2^{-\bullet}$ adduct was observed.[72] Purging of the reaction suspension with oxygen did not significantly increase the formation of the DMPO-$O_2^{-\bullet}$adduct, as either the solution was saturated with oxygen at the beginning or the surface-adsorbed oxygen in the photocatalyst exceeded the required amount; thus, the additional oxygen did not undergo the formation of $O_2^{-\bullet}$. Additionally, we performed a DMPO/H_2O experiment to follow the generation of $OH^\bullet$. We can observe in Figure S14b that in the dark conditions, no signal for the DMPO−$OH^\bullet$ adduct was observed (1:2:2:1 quartet signal). Illumination of the reaction suspension containing either the MRref or MR12 sample produced the DMPO−$OH^\bullet$ adduct, thus proving the generation of $OH^\bullet$, although its intensity was low. This could be attributed either to the lower tendency of the examined solids to form $OH^\bullet$ rather than other ROS or to the experimental conditions. However, the generation of $OH^\bullet$ from $O_2^{-\bullet}$ was proven by the results of experiments where coumarin (Figure 8a) and $ABTS^{\bullet+}$ (Figure 8b) were used as scavengers. This is discussed in detail in the Supporting Information.

All of the performed mechanistic studies are in agreement with the observed BPA quenching experiments (Figure 7c,d), from which we can conclude that the generation of $^1O_2$ and $O_2^{-\bullet}$ as the primary ROS is favored and that the $OH^\bullet$ radicals are generated only in minor quantities and as such do not significantly contribute to the photooxidation of organic pollutants.

4. CONCLUSIONS

Using the Simplex optimization method, we optimized the synthesis conditions for thermal polymerization and prepared several g-C_3N_4-based photocatalysts (MR1−15). Compared to the traditional stepwise optimization technique, we quickly obtained an improved g-C_3N_4 photocatalyst with a larger S_{BET}. The S_{BET} increased from 16 m^2/g (MRref sample) and 19 m^2/g (commercial TCI) to 86 m^2/g (MR12 solid), which is atypical for the g-C_3N_4 precursor dicyandiamide used. Structural investigation of the three most promising candidates (MR5, MR12, and MR15 samples) revealed that all samples have characteristic stretching and vibrational modes of g-C_3N_4 (FTIR analysis) and that the structure consists of the tri-*s*-triazine motif, as revealed by NMR analysis. The Simplex optimization method improved not only the S_{BET} but also the crystallinity (decreased *d*-spacing from 0.325 to 0.320) and reduced the thickness of the material as shown by TEM analysis (5−7 layers for MRref to a single-foil layer for MR12). This allowed the presence of quantum size effects, which are evident in the changes in optical properties (increase in E_g^{opt} to 2.95 eV compared to 2.63 eV for MRref) and electronic properties (decrease in R_{CT} from 4.46 MΩ for MRref to 2.64 MΩ for MR12) of the obtained g-C_3N_4 materials. Moreover, the "harsh" Simplex synthesis conditions encapsulated the DCDA precursor and burned it to gaseous products, leading to the formation of defects (pores) with the remaining NH_x functional groups. By using different temperature-programmed techniques, we found that these functional groups were indeed "trapped" in the layered structure, as they did not interact with the probe molecules. However, an extension of the lifetime of the charge carriers was observed, as these defects can act as electron traps and prevent the recombination of the charge carriers. It should be noted that a higher number of defects, as in the case of the MR15 sample, can act as recombination centers for charge carriers and thus reduce the lifetime of the charge carriers. This was confirmed by the solid-state

https://doi.org/10.1021/acscatal.3c03394
ACS Catal. 2023, 13, 13282−13300

photoluminescence and EPR analyses, where the MR15 photocatalyst ($\tau_{average}$ = 11.8 ns) had a shorter charge carrier lifetime than, for example, the MR12 solid ($\tau_{average}$ = 12.7 ns), as its defect content was the highest (highest EPR signal). Due to these structural and textural features, the MR12 sample exhibited the most favorable balance between all studied parameters, with a reduced charge transfer resistance (2.64 MΩ) and an enhanced photocurrent response (highest value of 627 $\mu A/cm^2$) with a prolonged relaxation time. As the lifetime of the charge carriers was prolonged, the MR12 material utilized the charge carriers to a higher extent than the other studied materials, resulting in (i) the highest BPA photooxidation rate (100%), (ii) the highest degree of BPA mineralization ($TOC_{mineralization}$ = 28.0%), and (iii) high photocatalytic stability (about 9% activity loss after five cycles). By using different quenching agents, we confirmed that in the case of the MR12 photocatalyst, the ROS that are responsible for the degradation of BPA are $^1O_2$ and $O_2^{-\bullet}$, proving the synergistic effect between the photooxidation of free and unfree radicals and the similar behavior of the photocatalyst toward organic macromolecules (e.g., Rose Bengal). This synergistic effect of type I and II sensitizers normally requires a metallic compound, but we achieved this phenomenon only with an environmentally friendly polymeric material (g-C_3N_4). In comparison, in the case of the MRref sample, the main ROS is only $O_2^{-\bullet}$ due to its thicker structure and lower S_{BET}. This restricts quantum confinement effects and limits the formation of $^1O_2$ in addition to its poorer optical and electronic properties. The enhanced formation of $^1O_2$ enabled the MR12 photocatalyst to successfully degrade BPS (13.9%) and BPAF (20.7%) to a higher extent than that of TiO_2/Au systems under visible-light (5 and 7% for BPS and BPAF, respectively). Furthermore, the generation of $^1O_2$ enabled the MR12 photocatalyst to selectively degrade the studied pharmaceutical compounds under visible light and showed the potential for "real-world" application as the degradation of BPA, BPS, and BPAF increased under simulated sunlight. By using TEMP and DMPO as spin traps as well as coumarin and $ABTS^{\bullet+}$ trap experiments, we were able to confirm the mechanistic conclusions from the BPA degradation experiments.

■ ASSOCIATED CONTENT

Supporting Information

The Supporting Information is available free of charge at https://pubs.acs.org/doi/10.1021/acscatal.3c03394.

Simplex theory discussion; environmental applications of photocatalysts discussion; temperature-programmed measurement result discussion; opto-electrochemical measurement result discussion; mechanistic study discussion; detailed experimental setup information; additional emission spectra of lights used; additional FTIR, TGA, TPD, ζ-potential, UV−vis-DR, CV, PL, EPR, EIS, TCSPC figures and tables; additional reusability test, degradation of various model pollutants under visible and solar illumination results (PDF)

■ AUTHOR INFORMATION

Corresponding Author

Gregor Žerjav − *Department of Inorganic Chemistry and Technology, National Institute of Chemistry, SI-1001 Ljubljana, Slovenia;* orcid.org/0000-0002-8934-8411; Phone: +386 1 47 60 249; Email: gregor.zerjav@ki.si

Authors

Matevž Roškarič − *Department of Inorganic Chemistry and Technology, National Institute of Chemistry, SI-1001 Ljubljana, Slovenia*

Janez Zavašnik − *Gaseous Electronics, Jožef Stefan Institute, SI-1000 Ljubljana, Slovenia;* orcid.org/0000-0002-8822-4089

Dániel Zámbó − *Centre for Energy Research, Institute of Technical Physics and Materials Science, H-1121 Budapest, Hungary;* orcid.org/0000-0001-7671-039X

Tomaž Kotnik − *Department of Inorganic Chemistry and Technology, National Institute of Chemistry, SI-1001 Ljubljana, Slovenia*

Sebastijan Kovačič − *Department of Inorganic Chemistry and Technology, National Institute of Chemistry, SI-1001 Ljubljana, Slovenia;* orcid.org/0000-0003-2664-9791

Albin Pintar − *Department of Inorganic Chemistry and Technology, National Institute of Chemistry, SI-1001 Ljubljana, Slovenia*

Complete contact information is available at: https://pubs.acs.org/10.1021/acscatal.3c03394

Notes

The authors declare no competing financial interest.

■ ACKNOWLEDGMENTS

This work was supported by the Slovenian Research Agency (research core funding no. P2-0150). The Slovenian Research Agency did not design, collect, analyze, or interpret any data and was not involved in the submission decision of the authors. Project no. TKP2021-NKTA-05 has been implemented with the support provided by the Ministry of Innovation and Technology of Hungary from the National Research, Development and Innovation Fund (NRDI), financed under the TKP2021 funding scheme. Moreover, this work was supported by the NRDI fund of Hungary under the grant of FK 142148. The authors would like to thank the companies Merel (Slovenia) and Horiba (Horiba France SAS) for their assistance in performing measurements of phosphorescence and QY.

■ REFERENCES

(1) Shi, Y.; Zhao, Q.; Li, J.; Gao, G.; Zhi, J. Onion-liked carbon-embedded graphitic carbon nitride for enhanced photocatalytic hydrogen evolution and dye degradation. *Appl. Catal., B* **2022**, *308*, No. 121216.

(2) Yang, F.; Chu, X.; Sun, J.; Zhang, Y.; Li, Z.; Liu, H.; Bai, L.; Qu, Y.; Jing, L. Efficient singlet oxygen generation by excitonic energy transfer on ultrathin g-C_3N_4 for selective photocatalytic oxidation of methyl-phenyl-sulfide with O_2. *Chin. Chem. Lett.* **2020**, *31*, 2784−2788.

(3) Wang, S.; Wang, J. Single atom cobalt catalyst derived from co-pyrolysis of vitamin B12 and graphitic carbon nitride for PMS activation to degrade emerging pollutants. *Appl. Catal., B* **2023**, *321*, No. 122051.

(4) Paušová, Š.; Baudys, M.; Kosina, J.; Praus, P.; Pintar, A.; Žerjav, G.; Roškarič, M.; Finšgar, M.; Krýsa, J. Photochemical stability of g-C_3N_4 in the gas phase. *J. Environ. Chem. Eng.* **2022**, *10*, No. 107647.

(5) Roškarič, M.; Žerjav, G.; Zavašnik, J.; Pintar, A. The influence of synthesis conditions on the visible-light triggered photocatalytic

activity of g-C_3N_4/TiO_2 composites used in AOPs. *J. Environ. Chem. Eng.* **2022**, *10*, No. 107656.
(6) Li, Y.; He, R.; Han, P.; Hou, B.; Peng, S.; Ouyang, C. A new concept: Volume photocatalysis for efficient H_2 generation - -using low polymeric carbon nitride as an example. *Appl. Catal., B* **2020**, *279*, No. 119379.
(7) Li, Y.; Ji, M.; Ma, Z.; Men, L.; He, R.; Peng, S. Hierarchically Porous Polymeric Carbon Nitride as a Volume Photocatalyst for Efficient H_2 Generation under Strong Irradiation. *Solar RRL* **2022**, *6*, No. 2100823.
(8) Zeng, D.; He, F.; Li, Y. Construction of terbium oxide/polymer carbon nitride heterojunction for boosting photocatalytic overall water splitting without cocatalyst. *Appl. Catal., A* **2023**, *650*, No. 118986.
(9) Bezerra, M. A.; dos Santos, Q. O.; Santos, A. G.; Novaes, C. G.; Ferreira, S. L. C.; de Souza, V. S. Simplex optimization: A tutorial approach and recent applications in analytical chemistry. *Microchem. J.* **2016**, *124*, 45−54.
(10) Sakkas, V. A.; Islam, M. A.; Stalikas, C.; Albanis, T. A. Photocatalytic degradation using design of experiments: A review and example of the Congo red degradation. *J. Hazard. Mater.* **2010**, *175* (1−3), 33−44.
(11) García Soto, A. R.; Rodríguez-Niño, G.; Trujillo, C. A. Zeolite LTA synthesis: Optimising synthesis conditions by using the modified sequential simplex method. *Ing. Investig.* **2013**, *33*, 22−27.
(12) Yasmin, C.; Lobna, E.; Mouna, M.; Kais, D.; Mariam, K.; Rached, S.; Abdelwaheb, C.; Ismail, T. New trend of Jebel Chakir landfill leachate pre-treatment by photocatalytic TiO_2/Ag nanocomposite prior to fermentation using *Candida tropicalis* strain. *Int. Biodeterior. Biodegrad.* **2020**, *146*, No. 104829.
(13) Amini, Z.; Givianrad, M. H.; Saber-Tehrani, M.; Azar, P. A.; Husain, S. W. Synthesis of N-doped TiO_2/SiO_2/Fe_3O_4 magnetic nanocomposites as a novel purple LED illumination-driven photocatalyst for photocatalytic and photoelectrocatalytic degradation of naproxen; optimization and different scavenger agents study. *J. Environ. Sci. Health, Part A* **2019**, *54*, 1254−1267.
(14) Nelder, J. A.; Mead, R. A simplex method for function minimization. *Comput. J.* **1965**, *7*, 308−313.
(15) Khummongkol, D.; Charoenkool, A.; Pongkum, N. Experimental optimization of activated carbon synthesis by the simplex search method. *Appl. Energy* **1992**, *41*, 243−249.
(16) Wrzecionek, M.; Howis, J.; Ruśkowski, P.; Gadomska-Gajadhur, A. Optimizing the conditions of PGSu synthesis with simplex method. *Chem. Eng. Process.* **2020**, *41*, 119−128.
(17) Cortés-Borda, D.; Wimmer, E.; Gouilleux, B.; Barré, E.; Oger, N.; Goulamaly, L.; Peault, L.; Charrier, B.; Truchet, C.; Giraudeau, P.; Rodriguez-Zubiri, M.; Grognec, E. L.; Felpin, F.-X. An Autonomous Self-Optimizing Flow Reactor for the Synthesis of Natural Product Carpanone. *J. Org. Chem.* **2018**, *83*, 14286−14299.
(18) Samsudin, M. F. R.; Bacho, N.; Sufian, S. Recent Development of Graphitic Carbon Nitride-Based Photocatalyst for Environmental Pollution Remediation. In *Nanocatalysts*; Sinha, I.; Shukla, M., Eds.; IntechOpen: London, United Kingdom, 2018. DOI: 10.5772/intechopen.81639.
(19) Rahman, M. M.; Shafiullah, A. Z.; Pal, A.; Islam, M. A.; Jahan, I.; Saha, B. B. Study on Optimum IUPAC Adsorption Isotherm Models Employing Sensitivity of Parameters for Rigorous Adsorption System Performance Evaluation. *Energies* **2021**, *14*, 7478.
(20) Cychosz, K. A.; Thommes, M. Progress in the Physisorption Characterization of Nanoporous Gas Storage Materials. *Engineering* **2018**, *4*, 559−566.
(21) Ma, L.; Wang, G.; Jiang, C.; Bao, H.; Xu, Q. Synthesis of core-shell TiO_2@g-C_3N_4 hollow microspheres for efficient photocatalytic degradation of rhodamine B under visible light. *Appl. Surf. Sci.* **2018**, *430*, 263−272.
(22) Zhu, B.; Xia, P.; Ho, W.; Yu, J. Isoelectric point and adsorption activity of porous g-C_3N_4. *Appl. Surf. Sci.* **2015**, *344*, 188−195.
(23) Yang, L.; Liu, X.; Liu, Z.; Wang, C.; Liu, G.; Li, Q.; Feng, X. Enhanced photocatalytic activity of g-C_3N_4 2D nanosheets through thermal exfoliation using Dicyandiamide as precursor. *Ceram. Int.* **2018**, *44*, 20613−20619.
(24) Zhang, J.; Chen, X.; Takanabe, K.; Maeda, K.; Domen, K.; Epping, J. D.; Fu, X.; Antonietti, M.; Wang, X. Synthesis of a Carbon Nitride Structure for Visible-Light Catalysis by Copolymerization. *Angew. Chem., Int. Ed.* **2010**, *49*, 441−444.
(25) Liu, Q.; Wang, X.; Yang, Q.; Zhang, Z.; Fang, X. A novel route combined precursor-hydrothermal pretreatment with microwave heating for preparing holey g-C_3N_4 nanosheets with high crystalline quality and extended visible light absorption. *Appl. Catal., B* **2018**, *225*, 22−29.
(26) Yan, Y.; Yang, M.; Wang, C.; Liu, E.; Hu, X.; Fan, J. Defected ZnS/bulk g−C_3N_4 heterojunction with enhanced photocatalytic activity for dyes oxidation and Cr (VI) reduction. *Colloids Surf., A* **2019**, *582*, No. 123861.
(27) Yan, H.; Zhu, Z.; Long, Y.; Li, W. Single-source-precursor-assisted synthesis of porous WO_3/g-C_3N_4 with enhanced photocatalytic property. *Colloids Surf., A* **2019**, *582*, No. 123857.
(28) Roškarič, M.; Žerjav, G.; Finšgar, M.; Zavašnik, J.; Pintar, A. Influence of the calcination duration of g-C_3N_4/TiO_2 "veggie-toast-like" photocatalyst on the visible-light triggered photocatalytic oxidation of bisphenol A. *J. Alloys Compd.* **2023**, *974*, No. 169585.
(29) Xia, P.; Cheng, B.; Jiang, J.; Tang, H. Localized π-conjugated structure and EPR investigation of g-C_3N_4 photocatalyst. *Appl. Surf. Sci.* **2019**, *487*, 335−342.
(30) Gao, D.; Xu, Q.; Zhang, J.; Yang, Z.; Si, M.; Yan, Z.; Xue, D. Defect-related ferromagnetism in ultrathin metal-free g-C_3N_4 nanosheets. *Nanoscale* **2014**, *6*, 2577−2581.
(31) Hu, Y.; Shim, Y.; Oh, J.; Park, S.; Park, S.; Ishii, Y. Synthesis of ^{13}C-,^{15}N-Labeled Graphitic Carbon Nitrides and NMR-Based Evidence of Hydrogen-Bonding Assisted Two-Dimensional Assembly. *J. Mater. Chem.* **2017**, *29*, 5080−5089.
(32) Wang, J.; Yin, S.; Zhang, Q.; Cao, F.; Xing, Y.; Zhao, Q.; Wang, Y.; Xu, W.; Wu, W.; Wu, M. Single-Atom Fe-N_4 sites promote the triplet-energy transfer process of g-C_3N_4 for the photooxidation. *J. Catal.* **2021**, *404*, 89−95.
(33) Jo, W.-K.; Natarajan, T. S. Influence of TiO_2 morphology on the photocatalytic efficiency of direct Z-scheme g-C_3N_4/TiO_2 photocatalysts for isoniazid degradation. *J. Chem. Eng.* **2015**, *281*, 549−565.
(34) Hao, R.; Wang, G.; Tang, H.; Sun, L.; Xu, C.; Han, D. Template-free preparation of macro/mesoporous g-C_3N_4/TiO_2 heterojunction photocatalysts with enhanced visible light photocatalytic activity. *Appl. Catal., B* **2016**, *187*, 47−58.
(35) Cui, L.; Fang, Z.; Liu, Y.; Chen, M.; Yin, C.; Wang, J.; Wang, Z.; Dong, M.; Kang, S.; Liu, P. Moderate $NaNO_2$ etching enables easy crystallinity optimization of g-C_3N_4 with superior photoreduction performance. *Inorg. Chem. Front.* **2019**, *6*, 1304−1311.
(36) LibreTexts Chemistry, X-ray diffraction (XRD) basics and application, Franklin & Marchall College, 2020 https://chem.libretexts.org/Courses/Franklin_and_Marshall_College/Introduction_to_Materials_Characterization__CHM_412_Collaborative_Text/Diffraction_Techniques/X-ray_diffraction_(XRD)_basics_and_application (accessed 10.12.2022).
(37) Jorge, A. B.; Martin, D. J.; Dhanoa, M. T. S.; Rahman, A. S.; Makwana, N.; Tang, J.; Sella, A.; Corà, F.; Firth, S.; Darr, J. A.; McMillan, P. F. H_2 and O_2 Evolution from Water Half-Splitting Reactions by Graphitic Carbon Nitride Materials. *J. Phys. Chem. C* **2013**, *117*, 7178−7185.
(38) Li, W.; Guo, Z.; Jiang, L.; Zhong, L.; Li, G.; Zhang, J.; Fan, K.; Gonzalez-Cortes, S.; Jin, K.; Xu, C.; Xiao, T.; Edwards, P. P. Facile *in situ* reductive synthesis of both nitrogen deficient and protonated g-C_3N_4 nanosheets for the synergistic enhancement of visible-light H_2 evolution. *Chem. Sci.* **2020**, *11*, 2716−2728.
(39) Etacheri, V.; Valentin, C. D.; Schneider, J.; Bahnemann, D.; Pillai, S. C. Visible-light activation of TiO_2 photocatalysts: Advances in theory and experiments. *J. Photochem. Photobiol., C* **2015**, *25*, 1−29.
(40) Chuang, P.-K.; Wu, K.-H.; Yeh, T.-F.; Teng, H. Extending the π-Conjugation of g-C_3N_4 by Incorporating Aromatic Carbon for

Photocatalytic H_2 Evolution from Aqueous Solution. *ACS Sustainable Chem. Eng.* **2016**, *4*, 5989−5997.
(41) Dvoranová, D.; Mazúr, M.; Papailias, I.; Giannakopoulou, T.; Trapalis, C.; Brezová, V. EPR Investigations of G-C_3N_4/TiO_2 Nanocomposites. *Catalysts* **2018**, *8*, 47.
(42) Cao, J.; Pan, C.; Ding, Y.; Li, W.; Lv, K.; Tang, H. Constructing nitrogen vacancy introduced g-C_3N_4 *p-n* homojunction for enhanced photocatalytic activity. *J. Environ. Chem. Eng.* **2019**, *7*, No. 102984.
(43) Savateev, A.; Pronkin, S.; Epping, J. D.; Willinger, M. G.; Wolff, C.; Neher, D.; Antonietti, M.; Dontsova, D. Potassium Poly(heptazine imides) from Aminotetrazoles: Shifting Band Gaps of Carbon Nitride-like Materials for More Efficient Solar Hydrogen and Oxygen Evolution. *ChemCatChem* **2017**, *9*, 167−174.
(44) Dong, G.; Jacobs, D. L.; Zang, L.; Wang, C. Carbon vacancy regulated photoreduction of NO to N_2 over ultrathin g-C_3N_4 nanosheets. *Appl. Catal., B* **2017**, *218*, 515−524.
(45) Zhang, D.; Wang, P.; Wang, J.; Zhan, S.; et al. Tailoring of electronic and surface structures boosts exciton-triggering photocatalysis for singlet oxygen generation. *Proc. Natl. Acad. Sci. U.S.A.* **2021**, *118*, No. e2114729118.
(46) Dong, F.; Li, Y.; Wang, Z.; Ho, W.-K. Enhanced visible-light photocatalytic activity and oxidation ability of porous graphene-like g-C_3N_4 nanosheets via thermal exfoliation. *Appl. Surf. Sci.* **2015**, *358*, 393−404.
(47) Liu, D.; Zhang, M.; Xie, W.; Sun, L.; Chen, Y.; Lei, W. Porous BN/TiO_2 hybrid nanosheets as highly efficient visible-light-driven photocatalysts. *Appl. Catal., B* **2017**, *207*, 72−78.
(48) Wu, C.; Han, Q.; Qu, L. Functional group defect design in polymeric carbon nitride for photocatalytic application. *APL Mater.* **2020**, *8*, No. 120703.
(49) Zhang, X.; Xie, X.; Wang, H.; Zhang, J.; Pan, B.; Xie, Y. Enhanced Photoresponsive Ultrathin Graphitic-Phase C_3N_4 Nanosheets for Bioimaging. *J. Am. Chem. Soc.* **2013**, *135*, 18−21.
(50) Ojha, D. P.; Karki, H. P.; Song, J. h.; Kim, H. J. Decoration of g-C_3N_4 with hydrothermally synthesized $FeWO_4$ nanorods as the high-performance supercapacitors. *Chem. Phys. Lett.* **2018**, *712*, 83−88.
(51) Pourshirband, N.; Nezamzadeh-Ejhieh, A.; Mirsattari, S. N. The CdS/g-C_3N_4 nano-photocatalyst: Brief characterization and kinetic study of photodegradation and mineralization of methyl orange. *Spectrochim. Acta, Part A* **2021**, *248*, No. 119110.
(52) He, Y.; Zhang, L.; Teng, B.; Fan, M. New Application of Z-Scheme Ag_3PO_4/g-C_3N_4 Composite in Converting CO_2 to Fuel. *Environ. Sci. Technol.* **2015**, *49*, 649−656.
(53) Yang, Y.; Guo, Y.; Liu, F.; Yuan, X.; Guo, Y.; Zhang, S.; Guo, W.; Huo, M. Preparation and enhanced visible-light photocatalytic activity of silver deposited graphitic carbon nitride plasmonic photocatalyst. *Appl. Catal., B* **2013**, *142*−*143*, 828−837.
(54) Fredrick, O. O.; Matoetoe, M. C. Electrochemical and optical band gaps of bimetallic silver-platinum varying metal ratios nanoparticles. *Afr. J. Pure Appl. Chem.* **2017**, *11*, 1−8.
(55) Holze, R. Optical and Electrochemical Band Gaps in Mono-, Oligo-, and Polymeric Systems: A Critical Reassessment1. *Organometallics* **2014**, *33*, 5033−5042.
(56) Chang, E.-C.; Chen, S.-A. Cyano-containing phenylene vinylene-based copolymer as blue luminescent and electron transport material in polymer light-emitting diodes. *J. Appl. Phys.* **1999**, *85*, 2057−2061.
(57) Ye, X.; Zhu, T.; Hui, Z.; Wang, X.; Wei, J.; Chen, S. Revealing the transfer mechanisms of photogenerated charge carriers over g-C_3N_4/$ZnIn_2S_4$ composite: A model study for photocatalytic oxidation of aromatic alcohols with visible light. *J. Catal.* **2021**, *401*, 149−159.
(58) Das, D.; Shinde, S. L.; Nanda, K. K. Temperature-Dependent Photoluminescence of g-C_3N_4: Implication for Temperature Sensing. *ACS Appl. Mater. Interfaces* **2016**, *8*, 2181−2186.
(59) Kočí, K.; Reli, M.; Troppová, I.; Šihor, M.; Kupková, J.; Kustrowski, P.; Praus, P. Photocatalytic decomposition of N_2O over TiO_2/g-C_3N_4 photocatalysts heterojunction. *Appl. Surf. Sci.* **2017**, *396*, 1685−1695.
(60) Hu, C.; Hung, W.-Z.; Wang, M.-S.; Lu, P.-J. Phosphorus and sulfur codoped g-C_3N_4 as an efficient metal-free photocatalyst. *Carbon* **2018**, *127*, 374−383.
(61) Shi, L.; Chang, K.; Zhang, H.; Hai, X.; Yang, L.; Wang, T.; Ye, J. Drastic Enhancement of Photocatalytic Activities over Phosphoric Acid Protonated Porous g-C_3N_4 Nanosheets under Visible light. *Small* **2016**, *12*, 4431−4439.
(62) Nadzwin Hasnan, N. S.; Mohamed, M. A.; Mohd Hir, Z. A. Surface Physicochemistry Modification and Structural Nanoarchitectures of g-C_3N_4 for Wastewater Remediation and Solar Fuel Generation. *Adv. Mater. Technol.* **2022**, *7*, No. 2100993.
(63) Kang, Y.; Yang, Y.; Yin, L.-C.; Kang, X.; Liu, G.; Cheng, H.-M. An Amorphous Carbon Nitride Photocatalyst with Greatly Extended Visible-Light-Responsive Range for Photocatalytic Hydrogen Generation. *Adv. Mater.* **2015**, *27*, 4572−4577.
(64) Žerjav, G.; Arshad, M. S.; Djinović, P.; Zavašnik, J.; Pintar, A. Electron trapping energy states of TiO_2−WO_3 composites and their influence on photocatalytic degradation of bisphenol A. *Appl. Catal., B* **2017**, *209*, 273−284.
(65) Žerjav, G.; Roškarič, M.; Zavašnik, J.; Kovač, J.; Pintar, A. Effect of Au loading on Schottky barrier height in TiO_2 + Au plasmonic photocatalysts. *Appl. Surf. Sci.* **2022**, *579*, No. 152196.
(66) Lu, W.; Xu, T.; Wang, Y.; Hu, H.; Li, N.; Jiang, X.; Chen, W. Synergistic photocatalytic properties and mechanism of g-C_3N_4 coupled with zinc phthalocyanine catalyst under visible light irradiation. *Appl. Catal., B* **2016**, *180*, 20−28.
(67) Dong, G.; Zhang, Y.; Pan, Q.; Qiu, J. A fantastic graphitic carbon nitride (g-C_3N_4) material: Electronic structure, photocatalytic and photoelectronic properties. *J. Photochem. Photobiol., C* **2014**, *20*, 33−50.
(68) Žerjav, G.; Teržan, J.; Djinović, P.; Barbieriková, Z.; Hajdu, T.; Brezová, V.; Zavašnik, J.; Kovač, J.; Pintar, A. TiO_2-β-Bi_2O_3 junction as a leverage for the visible-light activity of TiO_2 based catalyst used for environmental applications. *Catal. Today* **2021**, *361*, 165−175.
(69) Cojocaru, B.; Andrei, V.; Tudorache, M.; Lin, F.; Cadigan, C.; Richards, R.; Parvulescu, V. I. Enhanced photo-degradation of bisphenol pollutants onto gold-modified photocatalysts. *Catal. Today* **2017**, *284*, 153−159.
(70) Deng, Y.; Zhou, Z.; Zeng, H.; Tang, R.; Li, L.; Wang, J.; Feng, C.; Gong, D.; Tang, L.; Huang, Y. Phosphorous and kalium co-doped g-C_3N_4 with multiple-locus synergies to degrade atrazine: Insights into the depth analysis of the generation and role of singlet oxygen. *Appl. Catal., B* **2023**, *320*, No. 121942.
(71) Forchetta, M.; Valentini, F.; Conte, V.; Galloni, P.; Sabuzi, F. Photocatalyzed Oxygenation Reactions with Organic Dyes: State of the Art and Future Perspectives. *Catalysts* **2023**, *13*, 220.
(72) Xu, L.; Li, L.; Yu, L.; Yu, J. C. Efficient generation of singlet oxygen on modified g-C_3N_4 photocatalyst for preferential oxidation of targeted organic pollutants. *J. Chem. Eng.* **2022**, *431*, No. 134241.
(73) Peng, Y.; Xia, C.; Tan, Z.; An, J.; Zhang, Q. Size-controlled excitonic effects on electronic and optical properties of Sb_2S_3 nanowires. *Phys. Chem. Chem. Phys.* **2019**, *21*, 26515−26524.
(74) Sercel, P. C.; Lyons, J. L.; Bernstein, N.; Efros, A. L. Quasicubic model for metal halide perovskite nanocrystals. *J. Chem. Phys.* **2019**, *151*, No. 234106.
(75) Rettig, I. D.; McCormick, T. M. Enrolling reactive oxygen species in photon-to-chemical energy conversion: fundamentals, technological advances and applications. *Adv. Phys.: X.* **2021**, *6*, No. 1950049.
(76) Srivastava, A.; Singh, P. K.; Ali, A.; Singh, P. P.; Srivastava, V. Recent applications of Rose Bengal catalysis in N-heterocycles: a short review. *RSC Adv.* **2020**, *10*, 39495.
(77) Lim, J.; Kim, H.; Park, J.; Moon, G.-H.; Vequizo, J. J. M.; Yamakata, A.; Lee, J.; Choi, W. How g-C_3N_4 Works and Is Different from TiO_2 as an Environmental Photocatalyst: Mechanistic View. *Environ. Sci. Technol.* **2020**, *54*, 497−506.
(78) Nosaka, Y.; Nosaka, A. Y. Generation and Detection of Reactive Oxygen Species in Photocatalysis. *Chem. Rev.* **2017**, *117*, 11302−11336.

(79) Khan, A. U.SingletMolecular Oxygen. A New Kind of Oxygen. *J. Phys. Chem. A* **1976**, *80*, 2219−2228.
(80) Yarki, M. T.; Liu, B.; Tan, Y. N. Emerging Strategies in Enhancing Singlet Oxygen Generation of Nano-Photosensitizers Toward Advanced Phototherapy. *Nanomicro Lett.* **2022**, *14*, 123.
(81) Kang, S.; Fang, Y.; Huang, Y.; Cui, L.-F.; Wang, Y.; Qin, H.; Zhang, Y.; Li, X.; Wang, Y. Critical influence of g-C_3N_4 self-assembly coating on the photocatalytic activity and stability of Ag/AgCl microspheres under visible light. *Appl. Catal., B* **2015**, *168−169*, 472−482.
(82) Camussi, I.; Mannucci, B.; Spletini, A.; Profumo, A.; Milanese, C.; Malavasi, L.; Quadrelli, P. g-C_3N_4 - Singlet Oxygen Made Easy for Organic Synthesis: Scope and Limitations. *ACS Sustainable Chem. Eng.* **2019**, *7*, 8176−8182.
(83) Chen, D.; Kannan, K.; Tan, H.; Zheng, Z.; Feng, Y.-L.; Wu, Y.; Widelka, M. Bisphenol Analogues Other Than BPA: Environmental Occurrence, Human Exposure, and Toxicity-A Review. *Environ. Sci. Technol.* **2016**, *50*, 5438−5453.
(84) Saito, H.; Nosaka, Y. Mechanism of Singlet Oxygen Generation in Visible-Light-Induced Photocatalysis of Gold-Nanoparticle-Deposited Titanium Dioxide. *J. Phys. Chem. C* **2014**, *118*, 15656−15663.
(85) Wang, H.; Jiang, S.; Chen, S.; Li, D.; Zhang, X.; Shao, W.; Sun, X.; Xie, J.; Zhao, Z.; Zhang, Q.; Tian, Y.; Xie, Y. Enhanced Singlet Oxygen Generation in Oxidized Graphitic Carbon Nitride for Organic Synthesis. *Adv. Mater.* **2016**, *28*, 6940−6945.
(86) Dvoranová, D.; Barbieriková, Z.; Brezová, V. Radical Intermediates in Photoinduced Reactions on TiO_2 (An EPR Spin Trapping Study). *Molecules* **2014**, *19*, 17279−17304.
(87) Khachatryan, L.; Vejerano, E.; Lomnicki, S.; Dellinger, B. Environmentally Persistent Free Radicals (EPFRs). 1. Generation of Reactive Oxygen Species in Aqueous Solutions. *Environ. Sci. Technol.* **2011**, *45*, 8559−8566.

https://doi.org/10.1021/acscatal.3c03394
ACS Catal. 2023, 13, 13282−13300